24
12-9-80

LA-8537-SR

Status Report

Dr. 2106

1

R5H1

The Gyrocon Radio-Frequency-Generator Project for FY-78 and -79

MASTER

University of California

LOS ALAMOS SCIENTIFIC LABORATORY

Post Office Box 1663 Los Alamos, New Mexico 87545

LA-8537-SR
Status Report

UC-28
Issued: September 1980

The Gyrocon Radio-Frequency-Generator Project for FY-78 and -79

P. J. Tallerico
J. E. Rankin

DISCLAIMER

This book was prepared as an account of work sponsored by an agency of the United States Government. Neither the United States Government nor any agency thereof, nor any of their employees, makes any warranty, express or implied, or assumes any legal liability or responsibility for the accuracy, completeness, or usefulness of any information, apparatus, product, or process disclosed, or represents that its use would not infringe privately owned rights. Reference herein to any specific commercial product, process, or service by trade name, trademark, manufacturer, or otherwise, does not necessarily constitute or imply its endorsement, recommendation, or favoring by the United States Government or any agency thereof. The views and opinions of authors expressed herein do not necessarily state or reflect those of the United States Government or any agency thereof.

CONTENTS

THE GYROCON RADIO-FREQUENCY-GENERATOR PROJECT FOR FY-78 and -79

by

P. J. Tallerico and J. E. Rankin

ABSTRACT

The gyrocon is a high-power, high-efficiency amplifier that operates by deflection modulation of an electron beam. The bunching is better than that in a klystron, especially for very high powers and UHF frequencies, so the overall efficiency and the maximum output power can be higher than in a klystron. The present theory includes the effects of large signals, space charge, and finite beam size. The equations of motion are relativistically correct, and the space-charge fields are correct to first order in v/c. The theory is derived and a computer code to solve these equations is discussed. The code is then used to obtain several specific examples of gyrocon designs that have significant advantages over klystrons or gridded tubes in the 0.2- to 1.0-GHz frequency range.

Several embodiments of the gyrocon are possible, and we discuss the radial style and the spherical style in this report. The radial style has a bender magnet to increase the deflection of the beam, whereas the spherical gyrocon does not employ the bender magnet. The optimium frequency range for the spherical gyrocon is from 1.0 to 2.5 GHz.

The progress to date on the design, construction, and testing of a 650-kW output, 450-MHz prototype gyrocon is discussed. We had planned to have this gyrocon operating by the end of FY-79; however, two of the major subcontractors have had unexpected problems in producing the deflection and output cavities. The experimental program therefore will continue into FY-80. The sagacity of the early R & D investment, which proved the device feasibility by developing a sound theory and a prototype design, has been verified by receipt of funds from other agencies with urgent application needs.

I. INTRODUCTION

The gyrocon amplifier, shown in Fig. 1, consists of an electron gun, a focus coil, a deflection cavity, a bender and focus system, an output resonant ring, and a collector. The electron gun produces a solid beam that is focused by the focus coil. The beam is then deflected by the magnetic field of a TM_{110} resonator that is excited by two inputs that are displaced 90^{0} in space and time. The resultant magnetic field rotates at the rf drive frequency exactly like the magnetic field in a two-phase motor. After traversing the deflection cavity, the envelope of the beam describes a cone; although

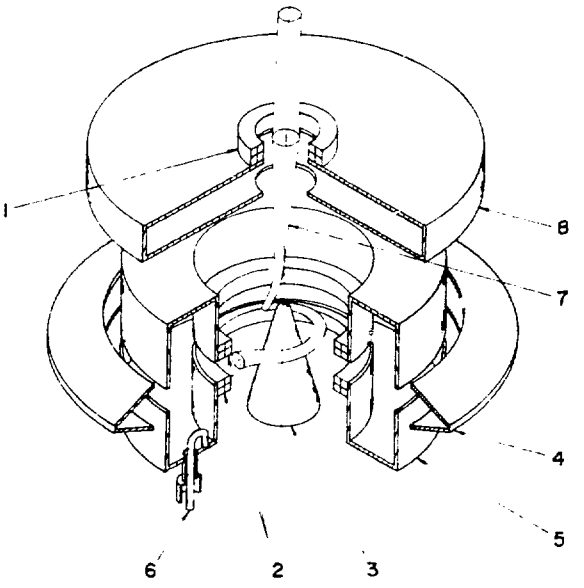

Fig. 1. The radial-style gyrocon:
(1) the first-focus coil,
(2) the output-focus coils,
(3) the conical-bender solenoid,
(4) the collector,
(5) the output cavity,
(6) of output line,
(7) the electron beam, and
(8) the deflection cavity.

each electron has only an r and z component of velocity, and the beam would appear as an expanding helix if it could be photographed. The beam then travels through a bender region that increases the deflection angle of the beam by a static magnetic field. In the figure, the bender field is from a conical bender solenoid. Next, a pair of oppositely excited coils focuses the beam toward the center of the output region, which is a section of coaxial line operating at resonance in the TE_{011} mode. The electrons give up their energy to the field as they cross the gap; if conditions are correct, over 90% of their kinetic energy can be transferred to the field. The collector simply is the beam stop, but it is usually designed to absorb the full power of the beam. The beam is decelerated by the radial component of the electric field in the resonator. The output fields are components of a fast wave, but because the azimuthal motion of the electrons is a deflection motion, the beam and the wave can be synchronous. The bunching in azimuth can be significantly better than the temporal bunching in a klystron, and we will show that operation is possible at very high beam voltages; thus large output powers are achievable.

Previous analytical studies[1,2] of the gyrocon deflection modulated rf amplifier have indicated that high dc-to-rf conversion efficiencies and acceptable gain and bandwidth for accelerator application can be achieved in the VHF to UHF frequency ranges. Two gyrocon devices have been built[3,4] in the Soviet Union; the first one produces 1-MW cw at 181 MHz, whereas the second is a low duty-cycle amplifier that produces 40 MW at 430 MHz. This second device drives the electron linac that feeds the VEPP-4[5] accelerator complex in Novosibirsk. The design theory[4] for these gyrocons is now available in

English. Recent analytical[6,7,8] work at the Los Alamos Scientific Laboratory (LASL) indicates that overall efficiencies over 80% can be realized from 100 MHz to 3 GHz with this type of amplifier. The efficiency increases as the output power is increased; thus the gyrocon is well suited for extremely high- power rf systems. With the gyrocon, cw output powers of more than 1 MW and pulse powers to 100 MW appear feasible.

The radial-style gyrocon shown in Fig. 1 has been studied under the auspices of the Department of Energy (DOE) and the Kirtland Air Force Weapons Laboratory (AFWL); 80% of the funding for FY-78 and FY-79 was from DOE. The objective of the DOE grant was to formulate a theory of the gyrocon, design a gyrocon, build a radial-style gyrocon and test it, all in the 2-yr time period. At the end of the 2-yr period, the first two tasks were completed and the construction of the gyrocon was proceeding both at LASL and at outside vendors. A test stand to do the gyrocon testing was ~75% complete. All fabrication orders were placed by Mar. 1979 and all parts were to be delivered by Sept. 15, 1979 so that some testing might take place at the end of FY-79. Unfortunately, the vendors of two major subassemblies, the output and deflection cavities, were more than 6 months late; the final assembly of the gyrocon could not begin until FY-80.

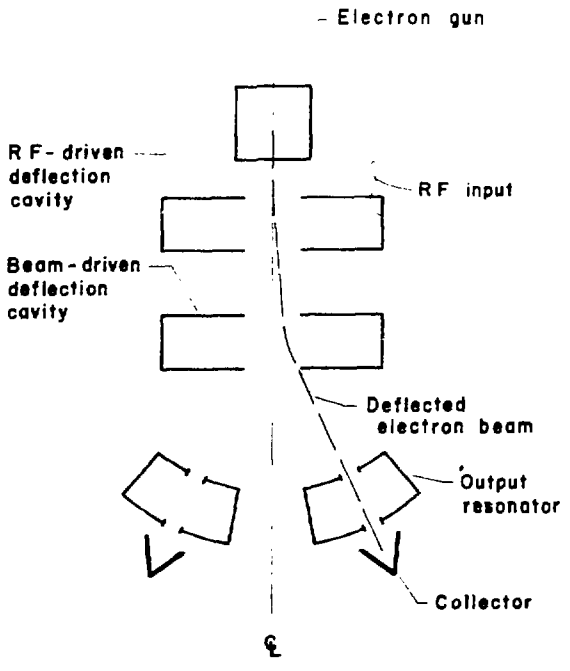

Fig. 2. The multiple-deflection cavity spherical gyrocon.

The AFWL was interested in refining the gyrocon principle to develop smaller, lighter devices. The theory of spherical output cavities, multiple deflection cavities (Fig. 2) and TE deflection modes, reported on pp. 30-38 below, was developed under AFWL sponsorship. Some preliminary work on a possible planar gyrocon was also done with this funding.

II. THE MATHEMATICAL MODEL

In the simplest terms, the gyrocon is composed of several coils, two rf cavities, and an electron beam to interact with these fields and its own space-charge fields. We analyze

the gyrocon by integrating the trajectory equations through various regions of the gyrocon. In this section the field equations and the equations of motion are derived and the assumptions are discussed. A fixed system of cylindrical coordinates is used for the analysis, and the trajectory equations are integrated, with time as the independent variable, through the static and dynamic fields that describe the gyrocon. Space-charge fields are included by a line-charge model that has been modified to take into account the effects of the spiral nature of the beam and of relativity. The rf fields are calculated for perfect, empty cavities. Thus it is assumed that the aperture and beam-loading effects on the cavities' fields are negligible.

A. Static Magnetic Fields

The static magnetic fields of the various coils are calculated by subdividing each coil into one or more current loops, and summing the fields for all the loops. The magnetic fields for an axially symmetric current loop may be shown[9] to be

$$B_r(r,z) = \frac{\mu_0 i_i (z - z_i)}{2\pi r \left[(r_i + r)^2 + (z_i - z)^2\right]^{1/2}} \times \left\{ \left[\frac{r_i^2 + r^2 + (z_i - z)^2}{(r_i - r)^2 + (z_i - z)^2} \right] E(m) - K(m) \right\}, \quad (1)$$

and

$$B_z(r,z) = \frac{\mu_0 i_i}{2\pi \left[(r_i + r)^2 + (z_i - z)^2\right]^{1/2}} \times \left\{ \left[\frac{r_i^2 - r^2 - (z_i - z)^2}{(r_i - r)^2 + (z_i - z)^2} \right] E(m) + K(m) \right\}, \quad (2)$$

where i_i is the ampere turns of the ith loop, r_i is the radius of the ith loop, z_i is the axial position of the ith loop, and K(m) and E(m) are the complete elliptic integrals of the first and second kind of the parameter m,

where

$$m = 4rr_i / \left[(r_i + r)^2 + (z_i - z)^2\right] \quad . \tag{3}$$

These fields are added, to find the total static fields over a cylindrical magnetic grid, and the fields at each electron's position are linearly interpolated from the tables. Fast elliptic integral routines from Ref. 10 are used in this computation. When permeable material is used to shape the magnetic fields, as in the gun region, the POISSON computer code[11] is used to evaluate the magnetic fields and equivalent coils are determined from the calculated field on the axis.

B. The Deflection Cavity Fields

The deflection cavity is cylindrical and can support TM_{110} modes. Two such modes, 90^o apart in space and time, can be combined to produce the traveling-wave fields as follows:

$$E_z(r,\phi, z,t) = E_o J_1(k_d r) \cos(\omega t - \phi) \quad , \tag{4a}$$

and

$$B_r(r,\phi, z,t) = \frac{E_o}{r\omega} J_1(k_d r) \cos(\omega t - \phi) \quad , \tag{4b}$$

$$B_\phi(r, ,z,t) = -\frac{E_o k_d}{\omega} J_1'(k_d r) \sin(\omega t - \phi) \quad , \tag{4c}$$

where

$$J_1'(k_d r) = \frac{d}{d(k_d r)} J_1(k_d r) = J_o(k_d r) - \frac{J_1(k_d r)}{k_d r} \quad , \tag{5}$$

$$k_d = p_{11}/a_1 \quad . \tag{6}$$

The first root of $J_1(x) = 0$ is p_{11} and a_1 is the radius of the deflection cavity. The resonant wavelength of the deflection cavity is

$$\lambda = 2\pi a_1 / p_{11} \quad . \tag{7}$$

By integrating the tangential magnetic fields over the four surfaces of the cavity, the ohmic losses in the deflection cavity are

$$P_L = \pi R_s \left(\frac{E_0}{\eta_0}\right)^2 J_0^2(k_d a_1)\, a_1(a_1 + d) \quad , \tag{8}$$

where R_s is the skin-effect resistance of the cavity ($R_s = 0.00452\ \lambda^{-1/2}$ for copper), η_0 is the impedance of free space, and d is the length of the deflection cavity. The quality factor of the resonator is

$$Q_{od} = \frac{d\ \mu_0\ a_1 \omega}{2R_s(a_1 + d)} \quad . \tag{9}$$

The effect of the apertures is neglected in the field and loss expressions. We also neglect any effect of the beam in exciting other modes.

C. Output-Cavity Fields

The output resonator is considered to be a TE_{011} mode coaxial resonator. Three major assumptions are made of the fields; the effects of apertures are neglected, all higher order modes are neglected, and only the forward wave is considered in the interaction. Although the gyrocon can be used as a frequency multiplier, we will consider only the amplifier case here. This requires one azimuthal variation of the fields in the output guide.

Let a be the inner radius of the output wave guide and b be the outer radius. The radial electric field is the most important component, so that radial field at r = a is denoted by E_0 and the other components are expressed in terms of E_0. The solution of Maxwell's equations for the output cavity may be shown to be

$$E_r = \frac{aE_0}{r} F(r) \cos \gamma(z - \bar{z}) \cos (\omega t - \phi + \theta_0 + \bar{\phi}) \quad , \tag{10a}$$

$$E_\phi = ak_c E_0 F'(r) \cos \gamma(z - \bar{z}) \sin (\omega t - \phi + \theta_0 + \bar{\phi}) \quad , \tag{10b}$$

$$B_r = \frac{\gamma a E_0 k_c}{\omega} F'(r) \sin \gamma(z - \bar{z}) \cos (\omega t - \phi + \theta_0 + \bar{\phi}) \quad , \tag{10c}$$

$$B_\phi = \frac{a\gamma E_0}{r\omega} F(r) \sin \gamma(z - \bar{z}) \sin (\omega t - \phi + \theta_0 + \bar{\phi}) \ , \tag{10d}$$

and

$$B_z = \frac{-ak_c^2 E_0}{\omega} F(r) \cos \gamma(z - \bar{z}) \cos (\omega t - \phi + \theta_0 + \bar{\phi}) \ , \tag{10e}$$

where

$$F(r) = \frac{J_1(k_c r)N_1'(k_c b) - N_1(k_c r)J_1'(k_c b)}{J_1(k_c a)N_1'(k_c b) - N_1(k_c a)J_1'(k_c b)} \ , \tag{11a}$$

and

$$F'(r) = \frac{J_1'(k_c r)N_1'(k_c b) - N_1'(k_c r)J_1'(k_c b)}{J_1(k_c a)N_1'(k_c b) - N_1(k_c a)J_1'(k_c b)} \ . \tag{11b}$$

In Eq. (10), $\bar{z}$ denotes the position of the center plane of the output gap and θ_0 is the phase reference of the circuit wave. The values of k_c and γ are determined by the boundary conditions of the problem. The E_ϕ field must vanish at r = a and b, and k_c is determined from the first root of

$$J_1'(k_c a)N_1'(k_c b) - J_1'(k_c b)N_1'(k_c a) = 0 \ . \tag{11c}$$

The axial propagation constant γ is determined from the usual relation

$$\gamma^2 = k^2 - k_c^2 \ , \tag{11d}$$

where $k = \omega/c$. The axial extent of the cavity, L, is determined by

$$\gamma L = \pi \ . \tag{11e}$$

The variable $\bar{\phi}$ is the average azimuthal position of the beam electrons as the beam is about to enter the output cavity. Thus Eqs. (10) and (11) determine

the circuit fields in the output cavity in terms of the cavity geometry and the arbitrary field amplitude E_o and phase θ_o. In practice, E_o and θ_o are used as input parameters and are varied to maximize the overall efficiency.

Once again, the tangential magnetic fields may be integrated over the cavity walls and the output power losses and Q are

$$P_{LO} = \frac{\pi a^2 E_o^2 R_s}{2\pi^2 \mu_o} \left\{ F^2(b) \left[k_c^2 b \, (k_c^2 L + 2\gamma^2 b) + \gamma^2 \left(\frac{L}{b} + 2\right) \right] \right.$$

$$\left. + k_c^2 a \, (k_c^2 L - 2\gamma^2 a) + \gamma^2 (L/a + 2) \right\} , \qquad (12)$$

and

$$Q_{out} = \frac{k^2 \mu_o \omega L}{2R_s}$$

$$\times \frac{(k_c^2 b - 1) F^2(b) - (k_c^2 a^2 - 1)}{\left[k_c^2 b (k_c^2 L + + 2\gamma^2 b) + \gamma^2 \left(\frac{L}{b} + 2\right) \right] F^2(b) + k_c^2 a (k_c^2 L - 2\gamma^2 a) + \gamma^2 \left(\frac{L}{a} + 2\right)} . \qquad (13)$$

D. Space-Charge Fields

The space-charge fields are calculated with a rod model to minimize the computer time. The beam, at any instant of time, could appear as a conically expanding helix, although each electron's velocities are primarily in the r- and z-directions. We assume that electrons emitted at different times have identical trajectories except for a change in angle by $\omega\Delta t$, where Δt is the emission time difference. The space-charge field calculation is rather involved and is described in detail in Appendix A. The procedure is described here briefly. The previous position of a reference electron is carried, and its old position is corrected by the $\omega\Delta t$ correction. A vector between this old position and the present position is constructed and a plane perpendicular to this vector is calculated. The reference particle lies on this plane and all the other particles are projected onto the plane. Finally, each particle is assumed to represent a rod of charge and the electric fields between each rod are calculated. The magnetic fields are calculated from the electric

fields and the field components are projected back to the particle's true position. The linear charge densities of the rods are corrected for the spiral motion of the beam and the slowing down of the whole beam.

The major assumptions in this model are that retardation and radiation modifications in the space-charge fields, and all image charges are neglected. The model clearly breaks down when electrons are reflected or if the entire beam stops. The model has been thoroughly checked for nonrotating beams and the authors feel that the major effects of space charge are correctly accounted for.

E. The Force Equations

A single cylindrical coordinate system is used in this analysis. Because of the three-dimensional nature of the beam, the angular force equation must be integrated numerically. Let the position and velocity of the ith particle be denoted by r_i, ϕ_i, z_i and $\dot{r}_i$, $\dot{\phi}_i$ and $\dot{z}_i$. The three components of the force on the ith particle can be expressed as

$$F_{r_i} = \frac{-n}{\gamma_i} \left\{ E_{r_i} \left[1 - (\dot{r}_i/c)^2 \right] + r_i \dot{\phi}_i \left(B_{z_i} - \dot{r} E_{\phi_i}/c^2 \right) \right.$$

$$\left. -\dot{z}_i (B_{\phi_i} + \dot{r} E_{z_i}/c^2) \right\} + r\dot{\phi}_i^2 \quad , \tag{14a}$$

$$F_{z_i} = \frac{-n}{\gamma_i} \left\{ E_{z_i} \left[1 - (\dot{z}_i/c)^2 \right] + \dot{r}_i (B_{\phi_i} - \dot{z}_i E_{r_i}/c^2) \right.$$

$$\left. - r_i \dot{\phi}_i (B_{r_i} + \dot{z}_i E_{\phi_i}/c^2) \right\} , \tag{14b}$$

$$F_{\phi_i} = \frac{-n}{\gamma_i r_i} \left\{ E_{\phi_i} \left[1 - (r_i \dot{\phi}_i/c)^2 \right] - \dot{r}_i (B_{z_i} + r_i \dot{\phi}_i E_{r_i}/c^2) \right.$$

$$\left. + \dot{z}_i (B_{r_i} - r\dot{\phi}_i E_{z_i}/c^2) \right\} - 2 \dot{r}_i \dot{\phi}_i / r_i \quad , \tag{14c}$$

where $\eta = |e|/m_o$ is the magnitude of the electronic charge to mass ratio evaluated at rest and γ_i is the usual relativistic factor

$$\gamma_i = \left\{1 - \left[\dot{r}_i^2 + \left(r_i\dot{\phi}_i\right)^2 + \dot{z}_i^2\right]/c^2\right\}^{-1/2} . \tag{14d}$$

The energy equation,

$$\dot{\gamma}_i = \frac{-\eta}{c^2}\left(\dot{r}_i E_{r_i} + r_i\,\dot{\phi}_i\, E_{\phi_i} + \dot{z}_i\, E_{z_i}\right) , \tag{14e}$$

is also integrated and used to test for numerical accuracy in the integration of the other equations. The total fields acting on each electron are found by adding the rf space-charge fields and static magnetic fields to any rf fields that are present in the various regions of the gyrocon.

The formulation in Eq. (14) is used because of the simplicity of the static fields and the rf fields in this coordinate system. The ω/r_i terms in the azimuthal force equations cause problems on the axis, but these can usually be avoided by proper choice of the time-integration step. The codes use rectangular coordinates for the force equations if IRECT > 0, as discussed in Appendix B.

III. CALCULATION OF RADIAL-STYLE GYROCON PERFORMANCE

A. The Calculation Method

The performance of the gyrocon is calculated by computing the trajectories of a group of electrons through the various regions of the gyrocon. The electrons initially are distributed in a disk, and each electron represents a fixed amount of charge. The initial conditions may be set for an ideal beam, or electron data from Herrmannsfeldt's electron gun program[12] may be used. The usual configuration of the gyrocon is an input drift space, a deflection cavity, the second drift-space/bender region, the output cavity and a collector drift space. The solenoid fields and the space-charge fields are calculated in each region, and the deflection- or output-cavity fields are added in the appropriate regions. The trajectories are integrated with time as the independent variable, and separate time steps for the drift and rf

regions may be used. The major assumptions are that the effects of the apertures in the deflection and output cavities are neglected, and that the space-charge rods can adequately represent the beam.

The equations presented in Sec. II are used to find the electron trajectories, but we must define the rf drive power and the electronic and overall efficiencies to complete the analysis. The electrons gain energy from the deflection-cavity fields that is due to beam-loading effects; thus the total rf drive power is

$$P_{DRF} = P_L + P_{BL} \quad , \tag{15}$$

where the beam loading power is

$$P_{BL} = I_o V_o \left[\gamma_o - 1 - \frac{1}{M} \sum_{i=1}^{M} (\gamma_i - 1) \right] . \tag{16}$$

The sum in Eq. (16) is evaluated at the first time step after all of the electrons have left the input cavity. The electronic efficiency of the output cavity is evaluated in a similar manner,

$$\eta_{e_\ell} = \gamma_o - 1 - \frac{1}{M} \sum_{i=1}^{M} (\gamma_i - 1) \quad , \tag{17}$$

where the sum is now evaluated immediately after the last electron leaves the output cavity. The actual power is then

$$P_{out} = I_o V_o \eta_{e_\ell} - P_{Lo} \quad , \tag{18}$$

and the rf gain of the gyrocon is

$$G = P_{out}/P_{DRF} \quad . \tag{19}$$

The overall dc-to-rf conversion efficiency is defined as

$$\eta_{oa} = P_{out}/(I_o V_o + P_{DRF}) \quad , \tag{20}$$

in which we neglect the small amount of input power necessary to heat the cathode and drive the bender and focus coils.

The above equations complete the mathematical model of the gyrocon, and any gyrocon of the type illustrated in Fig. 1 may be analyzed. Time steps corresponding to 1 mm in the drift regions and 0.5^{o} of the rf cycle in the rf regions generally are used in the computations, and a typical run takes 15 s on the CDC 7600 computer. The code GYRO1 analyzes the radial-style gyrocon; instructions are included as Appendix B.

B. Electron Dynamics

The most serious problem in the radial gyrocon is the aberration arising from the bender solenoid. Figure 3 shows the projections of the trajectories onto the rz plane for the prototype. The aberration is evident by the large radial deflection of the inner electrons and by the reduced radial deflection

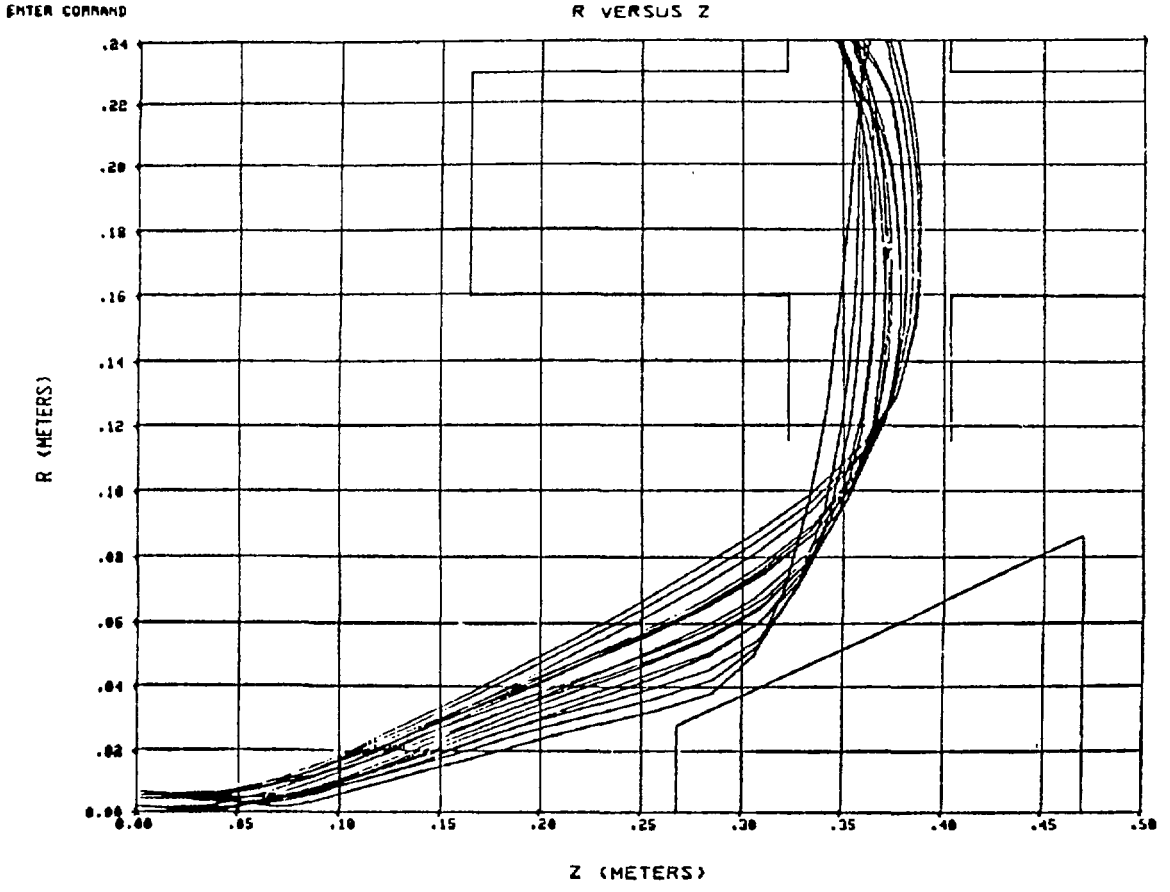

Fig. 3. Trajectories projected on the rz plane for the LASL gyrocon.

of the outer electrons. This aberration could result in a large spread in axial velocities as the beam traverses the output cavity and, therefore, result in lower efficiency. Another problem that is caused by the bender field aberration is shown in Fig. 4, the top view of the trajectories of the prototype gyrocon. The inner electrons execute more cyclotron motion than the outer electrons and this difference increases the azimuthal size of the beam. Both effects occur because the beam traverses the fringe field of the bender

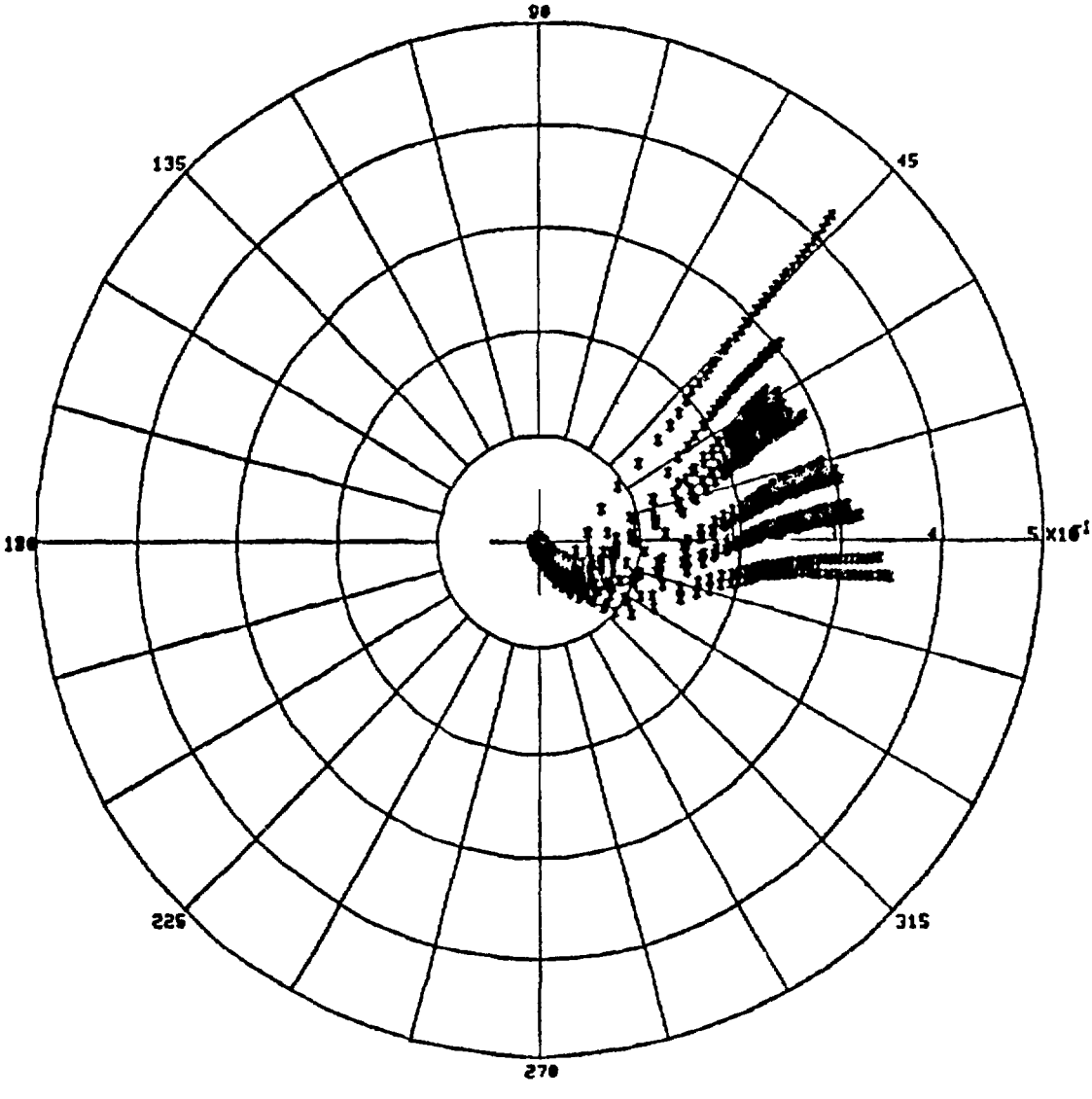

Fig. 4. Electron trajectories projected onto the rø plane.

solenoid, and these fields decrease quickly with distance. To obtain the highest possible efficiency, gyrocons should be designed to produce a beam minimum in the bender region.

The focus coils at the start of the output cavity reduce the angular spread in the rz plane, but also increase the azimuthal extent of the beam. In this case the beam in the output cavity is about 53° wide in azimuth, compared to about 110° in time for the bunch width in the best klystrons. It is this better bunching that results in such high electronic efficiencies for the gyrocon. The bunching improves with the beam voltage (at constant beam current), and the authors have obtained beam widths of 20° at 500 kV.

The beam spreads from space-charge forces and from any nonuniform radial velocities acquired in the deflection cavity. The space charge is relatively high in the prototype gyrocon; thus the optimum deflection angle is large and the rf gain is rather low. The rf forces in the output waveguide produce a net change of angular momentum in the negative ϕ direction, because the rf angular momentum is in the opposite direction. The polarity of all the coils becomes important. It is essential that the cyclotron motion given to the beam by the bender be in the same direction as the power flow in the output waveguide; in the prototype calculations, we found that the efficiency could be raised by a small amount if the initial cyclotron motion given to the beam by the first-focus coil opposes the cyclotron motion produced by the bender. An additional pair of coils was put in the collector region to control the electron dynamics between the output cavity and collector.

Figure 5 shows another projection of the trajectories onto the rz plane and also includes contour lines of the magnetic field. The maximum magnetic fields anywhere on a trajectory are less than 0.02 T for the prototype gyrocon. Higher voltage devices need stronger magnetic fields, but the requirements are rather modest.

C. Limits to Radial Gyrocon Performance

Although the calculated efficiencies of the prototype devices are very impressive, the next question to be answered concerns the power and frequency regions over which such excellent performance may be expected. It is obvious that to stop an electron beam of fairly high voltage, above 50 kV or so, many kilowatts of rf are required. It also takes several kilowatts to deflect such a beam. Thus, output powers of tens or hundreds of kilowatts are required for high overall efficiency.

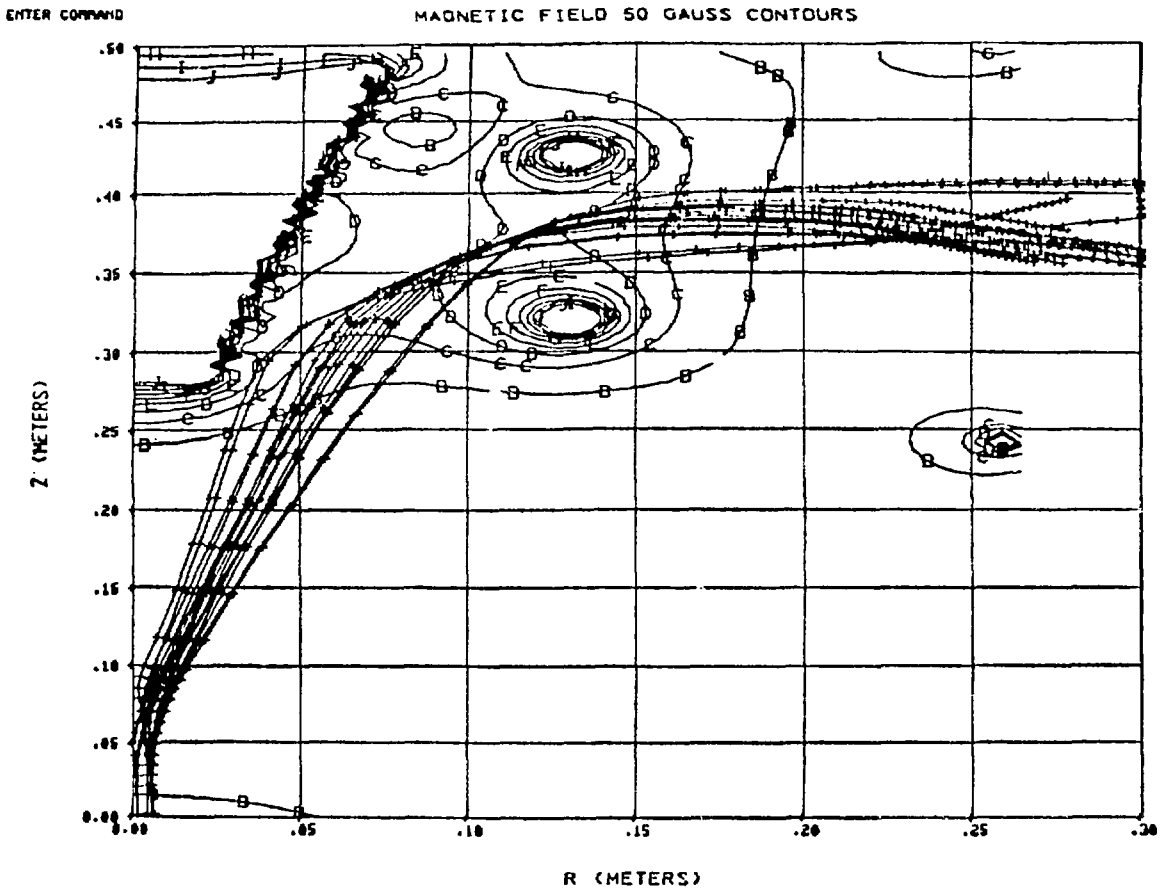

Fig. 5. Magnetic contours and electron trajectories on the rz plane for the prototype gyrocon.

The ideal method of optimizing gyrocon performance is to thoroughly explore the entire parameter space to find the maxima, as functions of beam voltage, current, frequency, and beam initial size. The parameter space is too large to conduct an effective search, because there are over 60 variables associated with the coils alone, and another dozen or more rf and geometric variables. The authors have made hundreds of computer runs trying to accomplish this rather difficult task, and we present the optimum results obtained so far, with the warning that for any particular case there may be a higher efficiency solution somewhere in the parameter space.

The major parameter search has been directed toward obtaining the highest overall efficiency as a function of beam voltage for several values of beam power. Table I shows the results for a frequency of 450 MHz and an

TABLE I

450-MHz GYROCON PERFORMANCE SUMMARY

WITH A 1-cm INITIAL BEAM RADIUS

V_o (kV)	I_o (A)	Dlen (cm)	E_{od} (MV/m)	P_{drf} (kW)	a (cm)	b-a (cm)	E_{oo} (MV/m)	θ_o (degrees)	Electronic Efficiency	P_l (kW)	Overall Efficiency	P_{out} (kW)	rf Gain
							100-kW Beam Power						
50	2.00	11	1.05	8.7	14	7.0	1.10	285	0.8872	10.6	0.7187	78.1	8.9
100	1.00	11	1.05	5.9	14	7.0	1.80	310	0.9026	28.3	0.5852	61.9	10.6
200	0.50	14	0.90	4.2	14	12.0	1.30	325	0.4803	23.1	0.2389	24.9	5.9
500	0.20	14	1.50	10.3	10	16.0	0.60	330	0.1026	2.0	0.0750	8.3	0.8
1000	0.10	8	2.10	17.3	14	18.0	0.30	320	0.0312	1.7	0.0126	1.5	0.1
							300-kW Beam Power						
50	6.00	11	1.30	26.9	17	7.0	1.15	280	0.8582	11.6	0.7522	245.9	8.9
100	3.00	11	1.30	12.8	14	7.0	2.15	305	0.9615	33.5	0.8149	254.9	19.8
200	1.50	16	1.00	8.2	9	8.0	3.50	325	0.9626	62.8	0.7332	226.0	27.5
500	0.60	14	1.65	13.3	10	18.0	4.10	320	0.7384	96.4	0.3993	125.1	9.4
1000	0.30	10	1.00	4.1	9	24.0	1.80	315	0.1945	19.5	0.1277	38.8	9.4
							1000-kW Beam Power						
100	10.00	10	1.80	42.1	14	7.0	2.05	315	0.9135	45.5	0.8329	868.0	20.6
200	5.00	18	0.70	10.7	10	10.0	3.40	315	0.9559	61.5	0.8848	894.4	83.0
500	2.00	11	1.80	15.5	10	16.0	5.85	315	0.9381	188.8	0.7378	749.3	48.3
1000	1.00	9	2.40	25.9	09	25.0	6.70	310	0.6863	149.2	0.3979	408.2	15.9
							3000-kW Beam Power						
100	30.00	6	3.60	113.2	14	7.0	2.05	310	0.8514	45.5	0.8058	2508.7	22.2
200	15.00	12	1.80	61.7	16	11.0	3.00	310	0.9269	77.3	0.8830	2703.3	43.8
500	6.00	12	1.70	20.3	13	16.0	5.80	310	0.9413	238.5	0.8560	2585.3	127.5
1000	3.00	9	2.40	24.1	14	18.0	7.30	315	0.7459	968.3	0.4197	1269.4	51.6
							10000-kW Beam Power						
200	50.00	20	1.50	684.5	13	7.0	4.00	320	0.8231	167.2	0.7548	8064.8	11.8
500	20.00	15	2.00	101.9	18	14.0	5.90	310	0.9426	359.5	0.8975	9067.3	88.9
1000	10.00	13	2.90	63.9	13	18.0	10.40	305	0.9644	824.7	0.8763	8819.3	137.9
2000	5.00	12	4.80	114.6	13	19.0	17.80	310	0.8647	2464.9	0.6112	6181.6	53.9

initial beam radius of 1.0 cm. These results show that the overall efficiency increases with an increase in the beam power. For any particular beam power, there is an optimum beam voltage, and this voltage also increases with beam power. The gyrocon performs better as the beam power is increased, but the power density or peak electric field allowable in the output gap establishes a maximum power limitation. The Soviet authors[4] suggest a maximum electric field of 10 MV/m in the cw case and 50 MV/m for the pulsed case. The peak fields in the output cavities of the gyrocons in Table I are all below 10 MV/m, with the exception of the 2000-kV, 5-A case.

A series of calculations also were made to determine the variation of the overall efficiency as the beam voltage was varied, and as the beam current was adjusted to keep the perveance constant. Table II shows the results of these computations. The overall efficiency increased under these conditions as the beam voltage was increased for the calculations, at a perveance of 3×10^{-8}. The overall efficiency was generally higher at the larger perveance of 3×10^{-7}, but the beam was more difficult to control because of the large space-charge forces. Some runs were made with a beam perveance of 1×10^{-6}, but the overall efficiency was low because of the large beam size at the output cavity. The authors estimate that the optimum beam perveance is within a factor of two of 3×10^{-7}. The gyrocon is thus a low-perveance device and one must work with high voltages to achieve the highest values of efficiency. The fundamental reason for the better performance at low perveance is the reduction in space-charge effects that significantly reduces the beam size, and the reduced beam size allows a higher electronic efficiency. The Soviet authors[4] have shown that, for a rectangular output waveguide in the limit of zero beam size and zero space charge, one can always find waveguide parameters that yield 100% electronic conversion efficiency.

A third series of calculations were made to determine the high-frequency limitation of the radial gyrocon. The beam initial radius was held at 1 cm and the beam voltage and current was held at 86 kV and 9.0 A for these calculations; Table III is a summary of the results. The beam size becomes larger, compared to the wavelength, as the frequency is increased and the electronic efficiency decreases. At 1200 MHz, the highest overall efficiency calculated for this type of gyrocon is only 52%, and it should be much easier to design a klystron with a higher efficiency at this and higher frequencies.

TABLE II

DEPENDENCE OF EFFICIENCY ON PERVEANCE FOR THE

450-MHz GYROCON WITH 1-cm INITIAL BEAM RADIUS

V_o (kV)	I_o (A)	D_{len} (cm)	E_{od} (MV/m)	P_{drf} (kW)	a (cm)	b (cm)	E_{oo} (Mv/m)	θ_o (degrees)	Electronic Efficiency	P_l (kW)	Overall Efficiency	P_{out} (kW)	rf Gain
							Perveance of 3×10^{-8}						
100	0.95	13	1.4	12.3	13	20	2.3	305	0.9406	35.9	0.4976	53.3	4.3
200	2.68	15	2.3	52.9	13	25	2.7	310	0.8843	50.3	0.7195	424.1	8.0
500	10.61	16	2.9	149.9	13	31	5.5	300	0.8499	230.2	0.7843	4277.2	28.5
1000	30.00	11	2.5	62.0	14	35	9.6	310	0.8850	1917.2	0.8194	24633.0	397.3
2000	84.85	8	7.8	400.7	21	44	16.1	300	0.8838	3796.4	0.8594	146190.0	364.8
							Perveance of 3×10^{-7}						
100	9.49	13	1.3	42.3	15	21	2.3	315	0.9166	40.8	0.8363	829.0	19.6
200	26.83	10	2.5	114.2	15	26	2.9	305	0.8872	66.9	0.8565	4694.0	41.1
500	106.07	10	6.4	1226.0	19	27	8.0	325	0.9128	639.9	0.8804	47769.0	39.0
1000	300.0	19	3.8	7085.0	13	29	10.5	325	0.8653	805.3	0.8427	258785.0	36.5
2000	848.53	13	12.2	27571.0	27	45	17 1	290	0.8127	5171.2	0.7967	1374029.0	49.8

TABLE III

EFFECT OF FREQUENCY ON GYROCON PERFORMANCE

(V_o = 86 kV, I_o = 9 A, r_o = 1-cm)

f (MHz)	D_{len} (cm)	E_{od} (MV/m)	P_{drf} (kW)	E_{oo} (MV/m)	θ_o (degrees)	b-a (cm)	Electronic Efficiency	Overall Efficiency	P_{out} (kW)	rf Gain
100	4.0	2.90	269.6	2.90	335	12.0	0.7204	0.4933	514.8	1.9
200	7.0	2.00	503.7	1.00	330	11.0	0.9017	0.8037	662.5	13.2
450	8.0	2.00	30.5	1.80	310	7.0	0.9184	0.8502	682.6	22.4
600	7.0	2.10	28.9	2.60	315	5.0	0.9155	0.8257	662.9	22.9
900	6.0	1.90	20.4	2.80	280	5.0	0.8174	0.7399	587.8	28.8
1200	8.0	2.30	650.1	3.40	255	5.0	0.7520	0.6429	539.4	8.3
1500	2.0	6.00	28.9	3.25	225	3.0	0.4666	0.4130	331.6	11.5

IV. THE LASL GYROCON DEMONSTRATION TUBE

A gyrocon is now under construction at the LASL to demonstrate the validity of the above radial-gyrocon theory and to test the radial-gyrocon concept. The frequency was fixed at 450 MHz by programmatic requirements for a proton accelerator, and the beam voltage was fixed at 86 kV, where a large power supply was available. A magnetic system was designed with POISSON, a magnet design code, to give a 9-A fairly laminar beam from an existing electron gun (Fig. 6). The trajectories were calculated with Herrmannfeldt's trajectory program.[12] The four beamlets shown in the figure were further subdivided by a factor of four in azimuth, and a gyrocon was designed to optimize the overall efficiency. An overall efficiency of slightly over 86% was achieved with the parameters listed in Table IV.

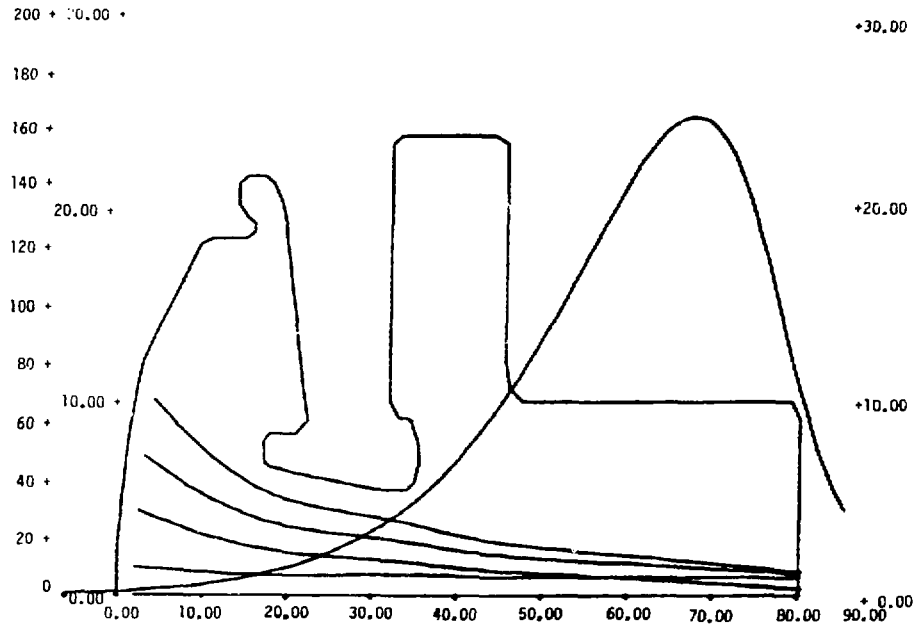

Fig. 6. Electron trajectories in the gun region of the LASL gyrocon.

TABLE IV

MAJOR PARAMETERS OF THE LASL GYROCON

Beam Voltage	86 kV
Beam Current	9.0 A
Deflection Angle	13.4°
Deflection Length	8.0 cm
Deflection Field	2.0 MV/m
Total Deflection Power	31.4 kW
First-Focus Coil Ampere Turns	-1540
Conical Bender Ampere Turns	14,000
Second-Focus Coil Ampere Turns	4000
Output Cavity, i.r.	16.8 cm
Output Cavity, o.r.	23.8 cm
Output Cavity Field	1.80 MV/m
Output Phase	310°
Electronic Efficiency	93.0%
Radio-frequency Gain	22.0
Overall Efficiency	86.1%
Output Power	691.9 kW

To optimize the gyrocon parameters, generally it is necessary to have the power lost in the output cavity equal to the total deflection power, and the two terms in the total deflection power must be approximately equal. This procedure tends to yield a highly efficient but low-gain design. The gain can be increased at the expense of efficiency, but the present device was designed for the highest dc-to-rf conversion efficiency.

Originally the prototype gyrocon was to be built of sheet metal and tested at very low average power to validate the mathematical model and to demonstrate the feasibility of the basic device. The mechanical engineering effort in such a device could be minimal. However, once the electron trajectories were calculated, it became clear that a well-cooled gyrocon would better survive errors in focus currents, or in drive levels, than would a sheet metal model. If the parts that are likely to be struck by electrons were made of heavy, water-cooled copper, the gyrocon could be tested with greater assurance that a slight error in setting one of the many experimental variables would not damage the gyrocon. Furthermore, informal discussion with members of the accelerator community and with people in the plasma heating community indicated that many high-efficiency, high peak-power, low average-power amplifiers (such as the magnetron and amplitron) exist. However, these rf users require high average power rf sources. A survey of the engineering problems associated with designing the prototype for high average power led us to conclude that it would be better to design the gyrocon for high average power. The chance of not finishing the project on time was perceived to be smaller than the risk of building a sheet metal gyrocon.

The overall electrical design of the prototype gyrocon was completed in the summer of 1978. Then the mechanical design phase began. Substantial heat flow calculations and mechanical deformation calculations were made. The results of some of these mechanical computations were inconsistant with the electrical design; more gyrocon calculations were made to determine the optimum compromise between the conflicting electrical and mechanical requirements. As this work continued, cold test models of the deflection and output cavities were built to empirically determine the optimum size of the coupling loops and tuners for these cavities. A total of six 2.5-cm-diam tuners were used in each cavity to place correctly the two degenerate circular

modes and to tune these modes to the correct frequency. Cold test models of the coaxial output lines and the coaxial-to-waveguide transducer were also built and tested. The conditions for a good output cavity rf match to the waveguide were found and incorporated into the mechanical design. Finally, early in calender 1979, ~ 100 D-size drawings were completed and the entire gyrocon was mechanically designed. By March 1979, all major components were either ordered from outside vendors or ordered from the LASL machine shops. The scheduled delivery dates were September 15, 1979 for the output and deflection cavities.

In the early summer the vendors who were supplying the output and deflection cavities indicated that they were experiencing difficulties in making these cavities. Both vendors wished to use low-temperature braze alloys rather than the higher melting point alloys specified on the drawings. Permission to make this substitution could not be granted because the high-temperature alloys had better vacuum properties that are essential to the gyrocon performance. A nickle-plating operation in the brazing process had been omitted from the LASL drawings and had to be added to the brazing procedure. Finally, after agreement on the brazing procedure was reached, rather lengthly discussion of the brazing jigs began. One of the 90-cm-diam end plates of the deflection cavity bowed from internal stresses after completion of the machining operations and another had to be built. The brazing and leak-checking operations on the deflection and output cavities had not been started by the subconstractors by the end of FY-79.

By the end of FY-79, the electron gun, the magnet components, the output ceramics, the input loops and cavity tuners, and the pinch-off manifold were complete and on hand at LASL. The collector assembly was 90% complete. Figures 7-12 show some of the subassemblies as they appeared in early 1980. The test stand, which consists of all the electrical equipment required to pulse the gyrocon and to protect it in case of a fault, was in place and the wiring was 30% complete. Several man-weeks of wiring and check-out were required to finish the stand. The test stand consists of eight 2-m-high racks of electronic gear, and all of this equipment has been built and tested individually. Figure 13 shows the test stand (photo early 1980). Thus, the experimental conformation of the gyrocon could not be attempted until FY-80.

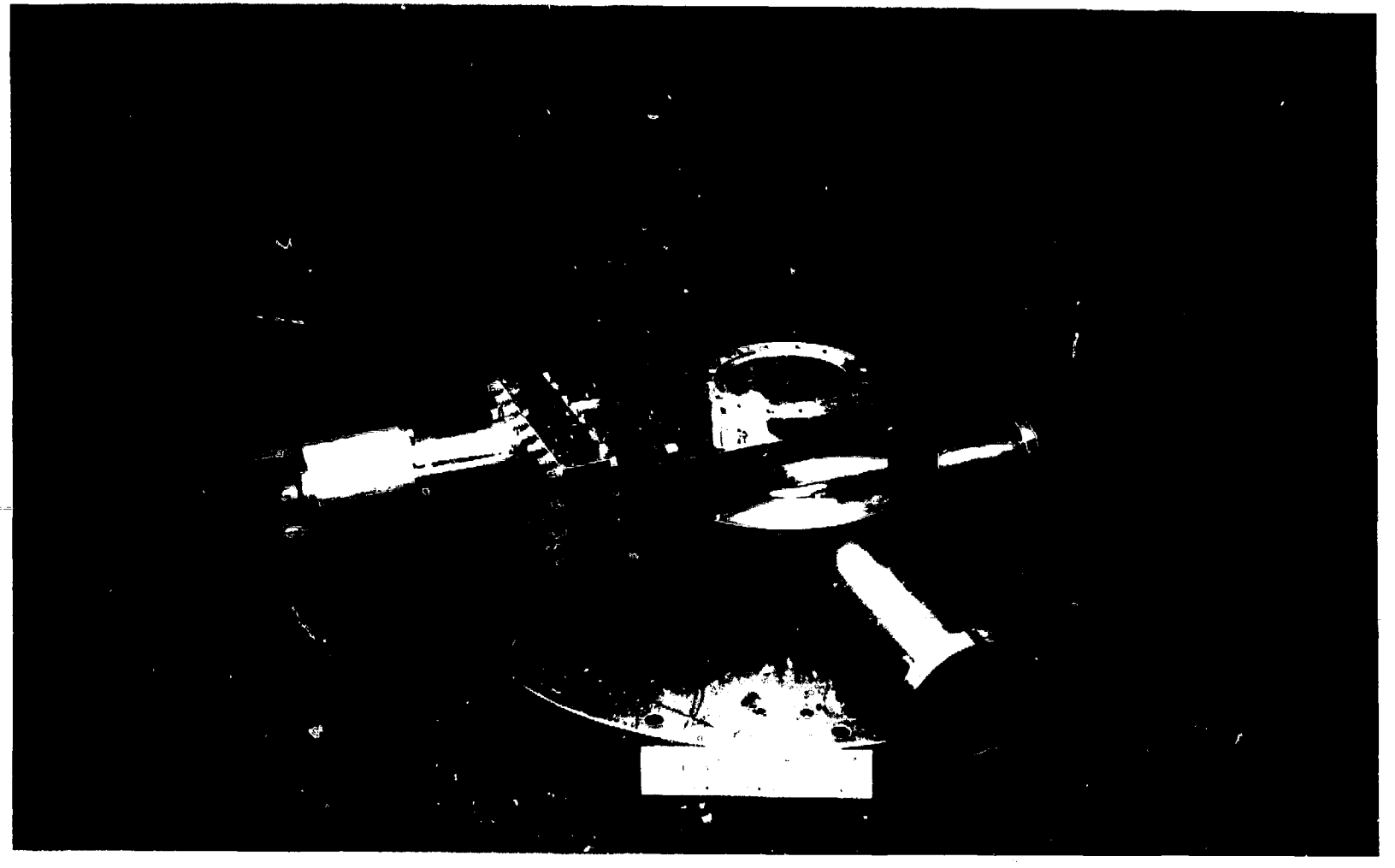

Fig. 7.
The mounting plate, vacuum valve,
and pump-out assembly.

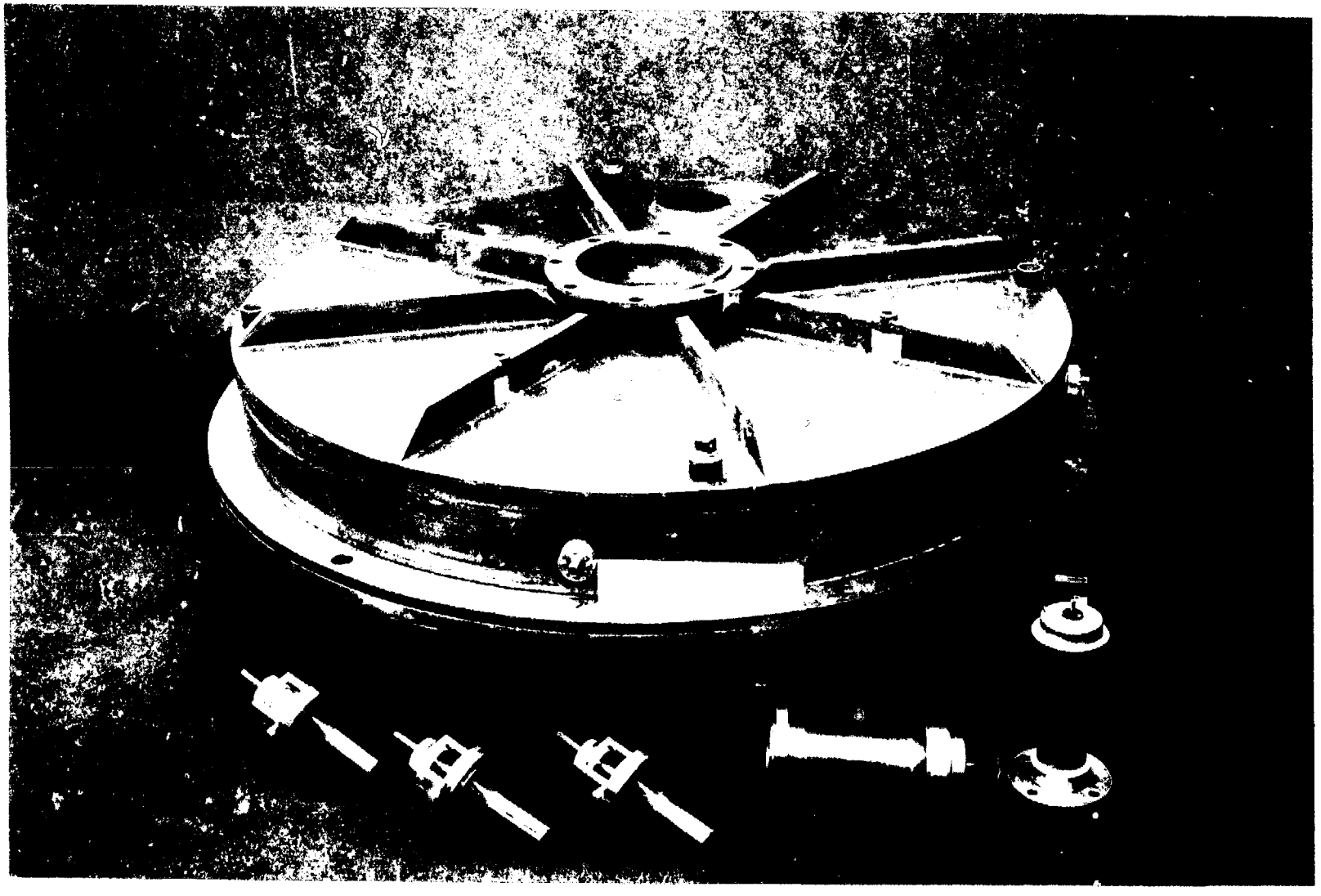

Fig. 8.
Deflection cavity with input loops
and tuners, prior to assembly.

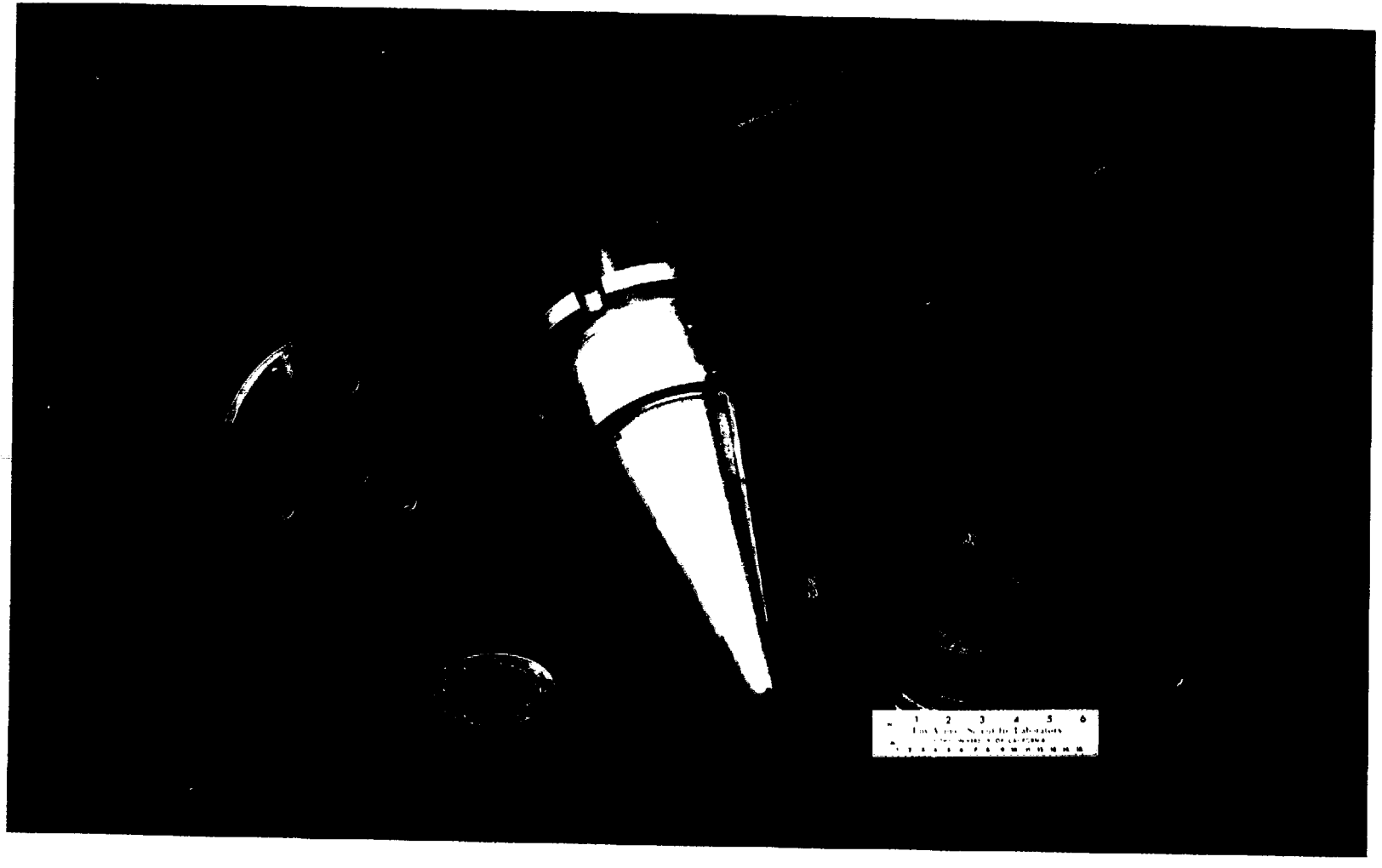

Fig. 9.
The conical bender magnet parts.

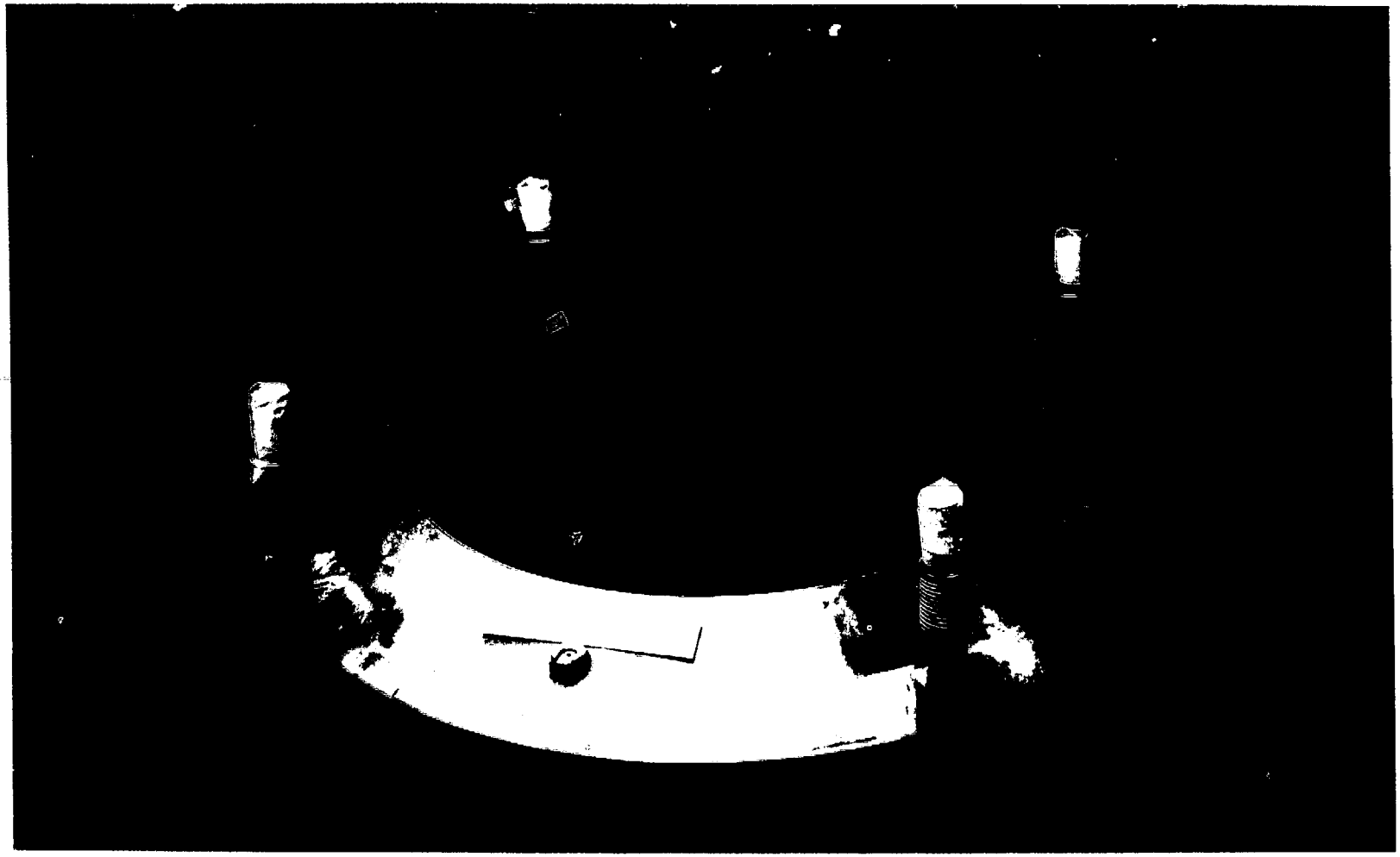

Fig. 10.
The collector assembly.

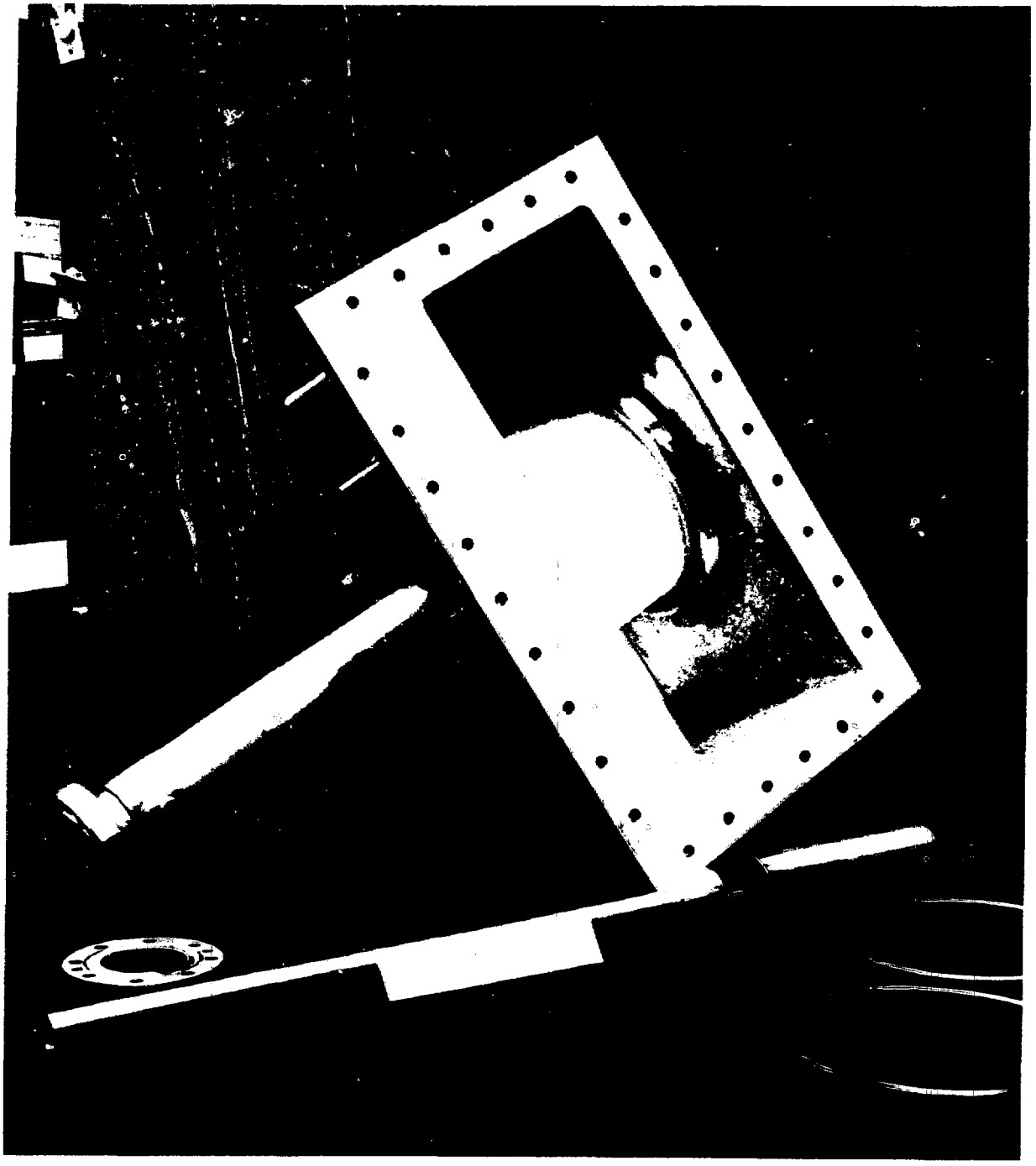

Fig. 11.
The output coaxial line and
coaxial-to-waveguide transducer.

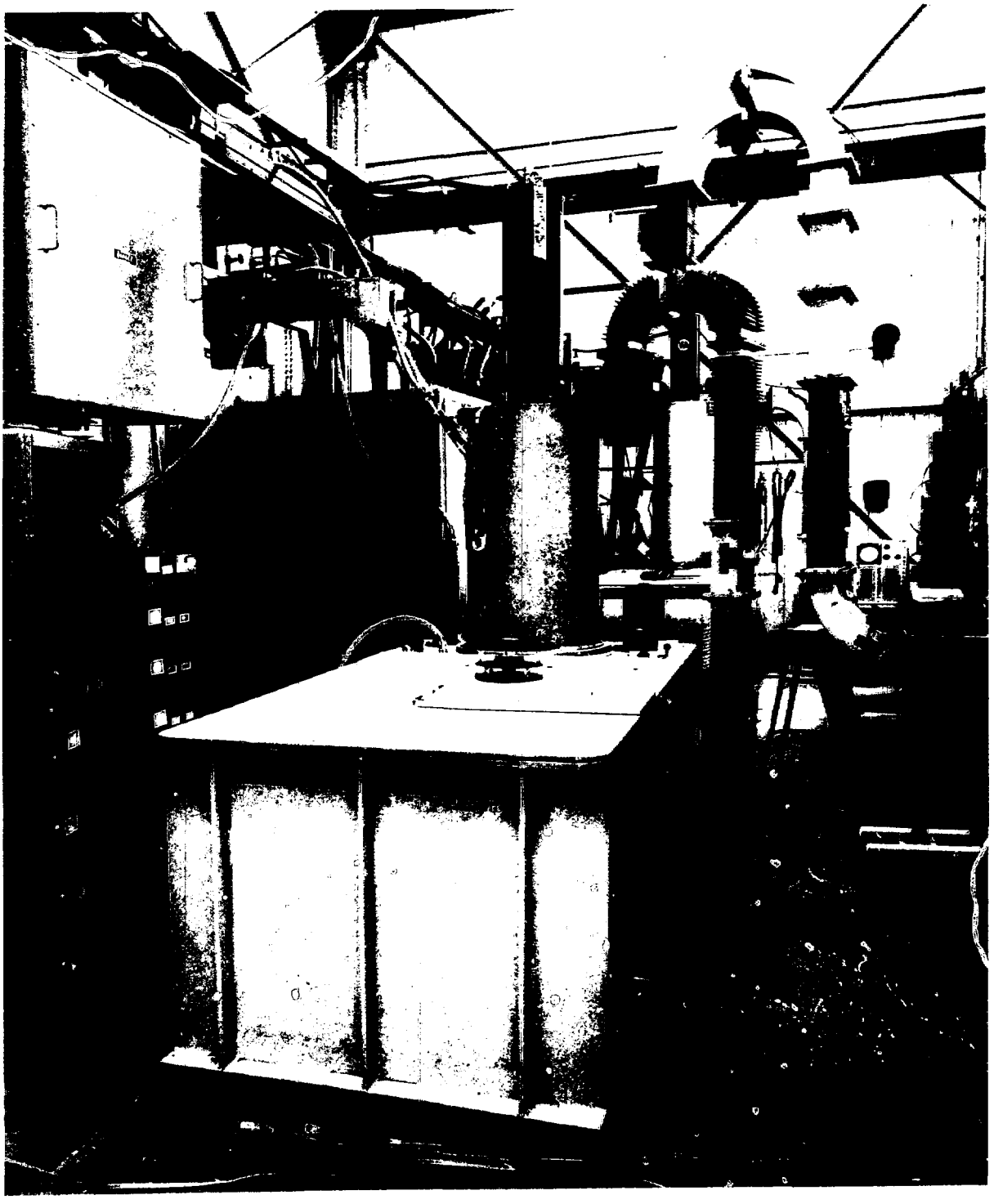

Fig. 12.
The gyrocon modulator with a klystron installed for modulator testing.

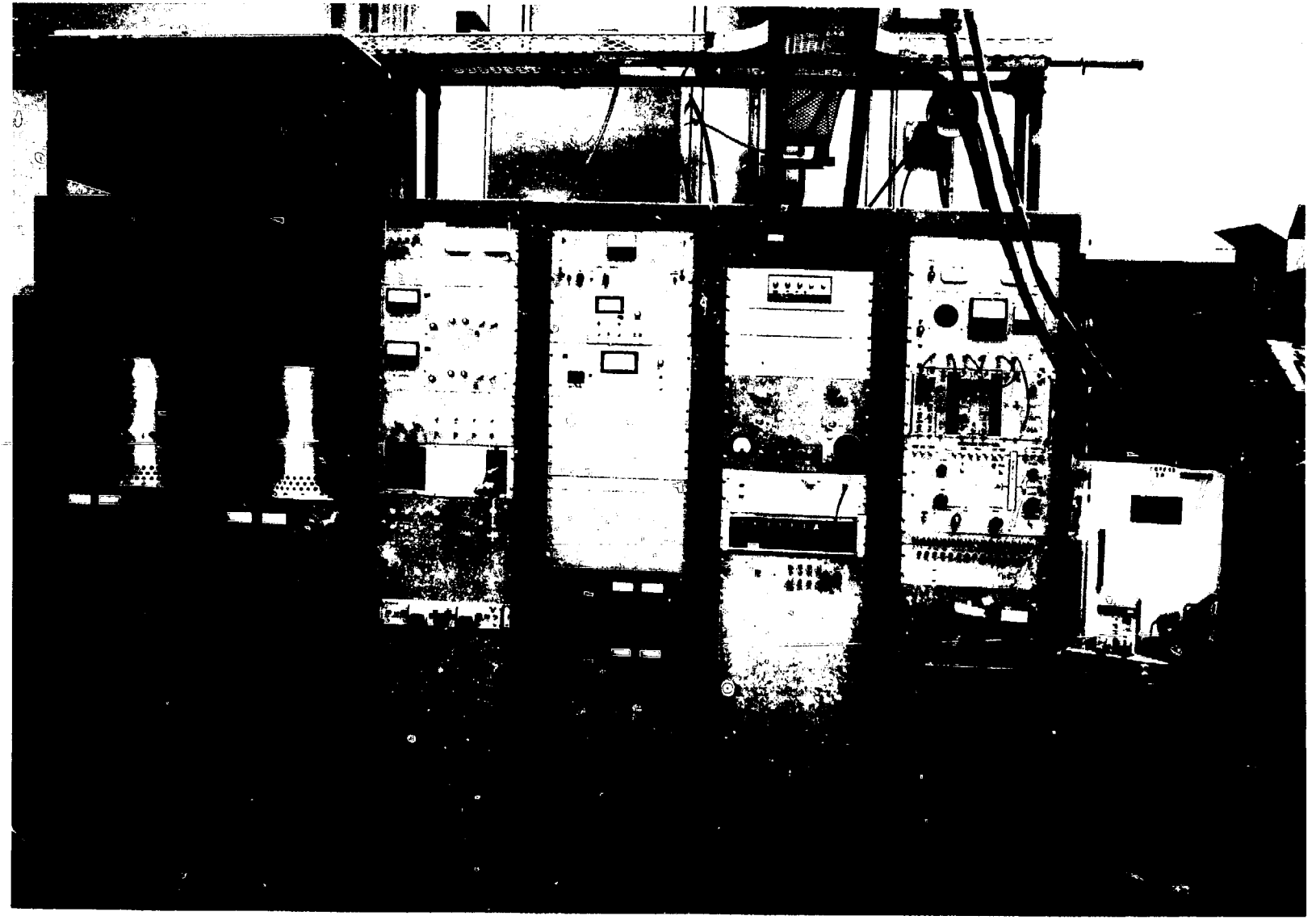

Fig. 13.
Gyrocon test stand, partial view.

However, the interest generated by the FY 1978-1979's theoretical and experimental progress in the accelerator, rf tube, DoD and other communities has resulted in additional support for the completion of this experimental phase, and for extension of the program to higher unit power tubes.

V. THE SPHERICAL GYROCON

It should be possible to improve the overall efficiency of the gyrocon at frequencies into the gigahertz region, if the bender case can be eliminated. The simplest method of eliminating the bender is to return to the original bermutron idea, but to use a spherical cavity, as shown in Fig. 2. The output cavity is a section of conical waveguide bounded by two concentric spheres, and the analysis is fairly straightforward, although complicated to reduce to code. The authors have analyzed this type of output cavity in the manner described in Ref. 13. In this section, we describe the results of the field analysis and then present some computed results, which show that the spherical gyrocon is a useful device up to the 2- to 3-GHz frequency range.

A. Mathematical Model

The output resonator is a section of conical waveguide bounded by two concentric spheres. If we neglect the effects of the slots, the fields (in spherical coordinates) may be shown to be

$$E_r = E_0(a^2/r^2)G(r)g(\theta)\cos[m(\omega t - \phi + \theta_0 + \bar{\phi})] \quad , \tag{21a}$$

$$E_\theta = \frac{E_0 a^2}{\ell(\ell+1)r} G'(r)g'(\theta)\cos[m(\omega t - \phi + \theta_0 + \bar{\phi})] \quad , \tag{21b}$$

$$E_\phi = \frac{mE_0 a^2}{\ell(\ell+1)r\sin\theta} G'(r)g(\theta)\sin[m(\omega t - \phi + \theta_0 + \bar{\phi})] \quad , \tag{21c}$$

$$B_\theta = \frac{mE_0 a^2}{\ell(\ell+1)r\sin\theta} (\omega/c^2)G(r)g(\theta)\cos[m(\omega t - \phi + \theta_0 + \bar{\phi})] \quad , \tag{21d}$$

$$B_\phi = \frac{E_0 a^2}{\ell(\ell+1)r}(\omega/c^2)G(r)g'(\theta)\sin[m(\omega t - \phi + \theta_0 + \bar{\phi})] \quad , \tag{21e}$$

and

$$B_r = 0 \quad \text{(TM modes)} \quad , \tag{21f}$$

where

$$G(r) = \frac{r}{ka^2}\,\frac{[\ell(\ell+1)n_\ell(ka) - kan_{\ell+1}(ka)]j_\ell(kr) - [\ell(\ell+1)j_\ell(ka) - kaj_{\ell+1}(ka)]n_\ell(kr)}{j_{\ell+1}(ka)n_\ell(ka) - n_{\ell+1}(ka)j_\ell(ka)} \tag{22a}$$

$$g(\theta) = \frac{P_\ell^m(-\cos\delta)P_\ell^m(\cos\theta) - P_\ell^m(\cos\delta)P_\ell^m(-\cos\theta)}{P_\ell^m(-\cos\delta)P_\ell^m(\cos\gamma) - P_\ell^m(\cos\delta)P_\ell^m(-\cos\gamma)} \tag{22b}$$

As before, the primes represent the derivatives with respect to the argument and we utilize the generalized associated Legendre functions and spherical Bessel functions

$$\begin{Bmatrix} j_\ell(x) \\ n_\ell(x) \end{Bmatrix} = \sqrt{\frac{\pi}{2x}} \begin{Bmatrix} J_{\ell+1/2}(x) \\ N_{\ell+1/2}(x) \end{Bmatrix} \quad , \tag{22c}$$

and

$$k = \frac{m\omega}{c} \quad , \tag{22d}$$

$$G'(r) = \frac{dG}{dr} \quad , \tag{22e}$$

$$g'(\theta) = \frac{dg}{d\theta} \quad , \tag{22f}$$

$$\frac{d}{dx}\begin{Bmatrix} j_\ell(x) \\ n_\ell(x) \end{Bmatrix} = \frac{\ell}{x}\begin{Bmatrix} j_\ell(x) \\ n_\ell(x) \end{Bmatrix} - \begin{Bmatrix} j_{\ell+1}(x) \\ n_{\ell+1}(x) \end{Bmatrix} , \tag{22g}$$

and

$$\frac{dP_\ell^m(x)}{dx} = \frac{\ell - m + 1}{x^2 - 1} P_{\ell+1}^m(x) + \frac{(\ell + 1)x}{1 - x^2} P_\ell^m(x) . \tag{22h}$$

In the above equation, m is the number of wavelengths in the output cavity. For the gyrocon amplifier, m = 1.

The boundary conditions require

$$G'(a) = G'(b) = 0 \tag{23a}$$

and

$$g(\delta) = g(\alpha) = 0 . \tag{23b}$$

The first condition gives

$$[\ell(\ell + 1)n_\ell(ka) - kan_{\ell+1}(ka)]j_\ell(kb) - [\ell(\ell + 1)j_\ell(ka) - kaj_{\ell+1}(ka)]n_\ell(kb) = 0 . \tag{24}$$

This is solved for ℓ. The result is generally nonintegral, and yields generalized Legendre functions in g(θ) rather than the familiar polynomials. This also means that $p_\ell^m(\cos\theta)$ and $p_\ell^m(-\cos\theta)$ are independent functions.

The second boundary condition is solved for τ, the cavity width.

Using

$$\alpha = \frac{2\gamma + \tau}{2} \quad , \tag{25a}$$

and

$$\delta = \frac{2\gamma - \tau}{2} \quad , \tag{25b}$$

gives

$$P_\ell^m(-\cos\frac{2\gamma - \tau}{2})\, P_\ell^m(\cos\frac{2\gamma + \tau}{2}) - P_\ell^m(-\cos\frac{2\gamma + \tau}{2}) P_\ell^m(\cos\frac{2\gamma - \tau}{2}) = 0 \quad . \tag{25c}$$

The center angle, γ, is already known as user-specified program input. As m approaches ℓ, the above condition fails to have physical solutions (τ too large).

Power losses and Q are found by a combination of analytical and numerical integration to be

$$P_{LO} = \frac{\pi\varepsilon_0^2 E_0^2 \omega^2 a^4 R_s}{[\ell(\ell+1)]^2} \left\{ (G^2(b) + 1)\, I_1 + \left[(g'(\alpha))^2 \sin\alpha + (g'(\delta))^2 \sin\delta \right] I_2 \right\} , \tag{26}$$

$$Q = \frac{\pi\omega\varepsilon_0 a^4 E_0^2}{2P_{LO}} \left\{ I_3 I_5 + \frac{I_1 I_6}{[\ell(\ell+1)]^2} \right\} , \tag{27}$$

where

$$I_1 = \int_\delta^\alpha \left[\frac{m^2 g^2(\theta)}{\sin\theta} + \sin\theta (g'(\theta))^2 \right] d\theta \quad , \tag{28a}$$

$$I_2 = \int_a^b \frac{G^2(r)}{r}\, dr \quad , \tag{28b}$$

$$I_3 = \int_a^b \frac{G^2(r)}{r^2}\, dr \quad , \tag{28c}$$

$$I_5 = \int_{\zeta}^{\alpha} \sin\theta g^2(\theta) d\theta \quad , \tag{28d}$$

and

$$I_6 = \int_a^b \left[k^2 G^2(r) + \left(G'(r)\right)^2 \right] dr \quad . \tag{28e}$$

These five integrals are all performed using the trapezoid rule.

B. Calculated Results for the Spherical Gyrocon

A separate computer code, GYROS, has been written to evaluate the field expressions in the previous section and to analyze the spherical gyrocon. The input parameters are very similar to those used for GYRO1, although a static magnetic field was added to the output region in GYROS. This static compensation field is more important in the spherical case than for the radial-style gyrocon. The input parameters for GYROS are also given in Appendix B.

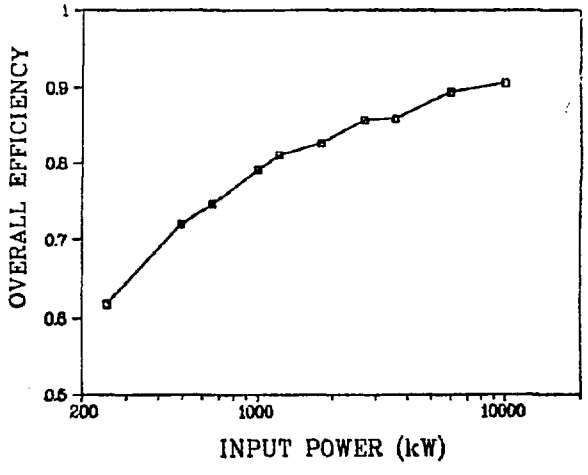

Fig. 14. Overall efficiency vs dc beam input power for the spherical gyrocon.

We have made a limited parameter search of spherical gyrocon characteristics, using the LASL code GYROS. At 2.45 GHz (the solar power satellite frequency) we find increasing overall efficiency, with increasing input power (Fig. 14). The microperveance for these runs is about 0.1, which makes the gyrocon a low-preveance device. The efficiency curve is roughly logarithmic, and electronic efficiencies of over 97% are predicted for the higher input powers. Output-cavity wall losses, at 1.8-MW input, average about 350 W/cm^2.

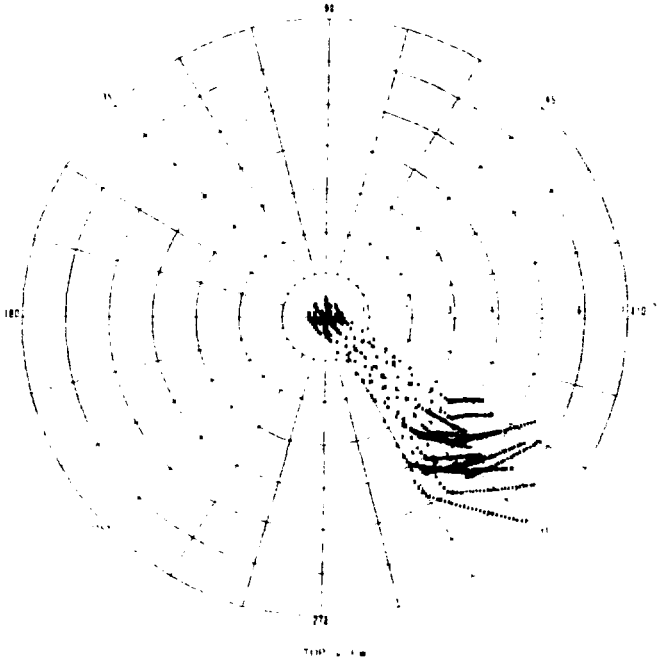

Fig. 15. Top view of the trajectories for the spherical gyrocon on the rø plane.

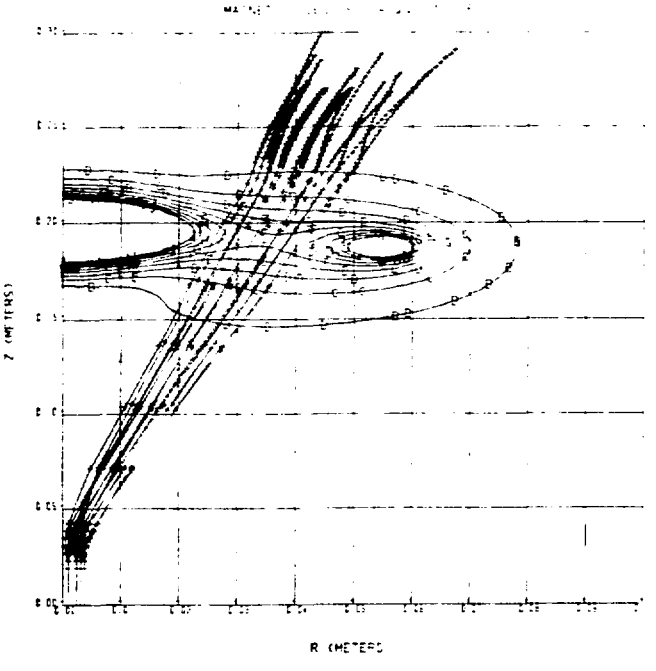

Fig. 16. Projection of spherical gyrocon trajectories onto the rz plane and 50-G magnetic contours from output-cavity focus coils.

Total output-cavity losses are about 172 kW. Figures 15,16 and 17 show various projections of the path formed by the passage of a single layer of electrons through the device at 1.8-MW input. These also show the output-cavity outline, and the output-cavity beam-focusing fields. The very narrow beam bunching shows clearly on the rø-plane projection. The static, magnetic, compensating field is not shown, but is roughly 200 G in the negative theta direction. Overcompensation here seems to produce improved efficiency.

In the 1.8-MW simulation, tube parameters include 70-kW drive power, an output-cavity Q over 11 000, an initial beam radius of 4 mm, a deflection angle of 11.9^{o}, and an output power of 1.55 MW. Output power is taken from pairs of output lines with internal separations of 90^{o} in each pair. The phasing of paired outputs is necessary to maintain the correct output-cavity traveling wave.

Also we have made a series of simulations of a tube of 1.8-MW input power at several frequencies. The graph of

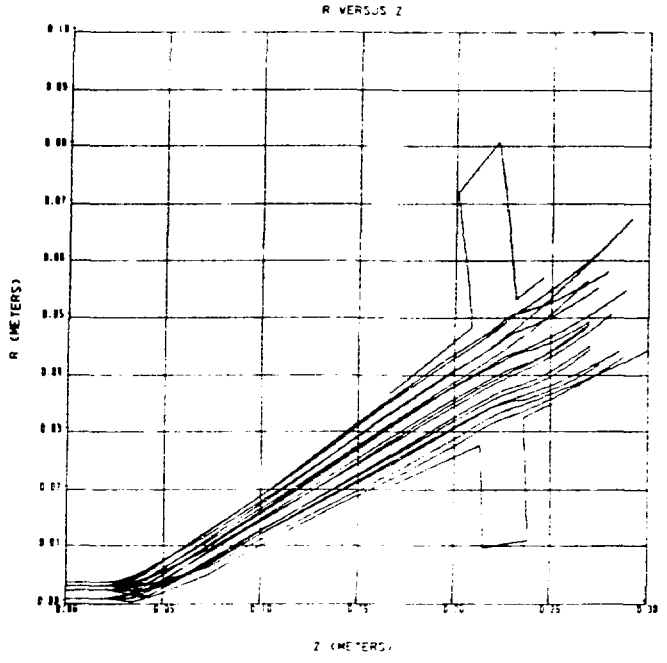

Fig. 17. Projection of the spherical gyrocon trajectories onto the rz plane with the outline of the output cavity.

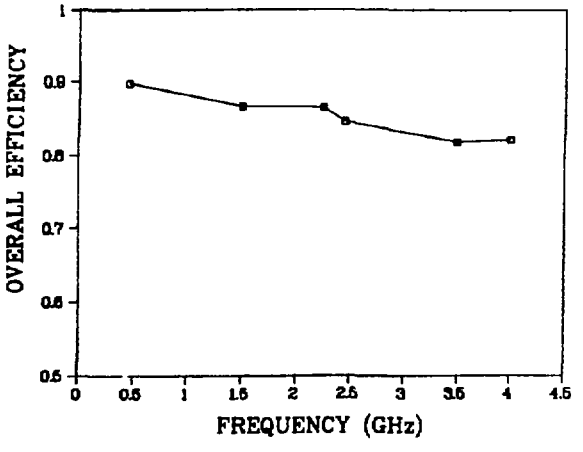

Fig. 18. Overall efficiency vs frequency for the spherical gyrocon with 1.8-W input power.

overall efficiency versus frequency (Fig. 18) shows a slow rise in efficiency as the frequency is lowered. Thus, the sphercial gyrocon is a viable generator into the several-GHz frequency region. The ever-diminishing size of the output cavity would make operation above 3 GHz impossible without heroic cooling techniques.

VI. PROBLEMS REMAINING AND SUGGESTIONS FOR FUTURE WORK

The code-development work at LASL will be directed towards removing some of the assumptions made in the present codes. Work has begun on the estimation of the aperture fringe fields in the output cavity, using both the electrostatic approximation and SUPERFISH output. These fringe fields are expected to be quite important above 1 GHz, because the cavity slot width becomes an appreciable fraction of a wavelength at these high frequencies.

Both the radial and the spherical style of gyrocon show rather low power gain of 10 to 20 dB. We have done some work with a developmental version of GYRO1, which slows multiple deflection cavities to be analyzed. The second deflection cavity is

driven by the beam's modulation current only, just like the intermediate cavities in a klystron. The initial results show an increase in gain of 3 to 5 dB per cavity, but the overall efficiency remains the same, because some of the dc beam power is converted to deflection cavity energy. We feel that this type of calculation cannot be performed accurately unless we have a self-consistent cavity-field calculation. In this calculation, we would estimate a field amplitude and phase in a deflection or output cavity, then calculate the induced current in the cavity caused by the beam. Next, we would use the known cavity impedance to calculate the field's amplitude and phase. We would relax the solution and trace the particles through the field again. The method is used in klystrons[14], but it is a bit more complicated in gyrocon applications. This self-consistant analysis would give the cavities' frequency detuning by the bunched beam.

Another area that has only been touched on by our work so far is the use of TE deflection modes. We have examined some candidate structures with the code SUPERFISH and tested a structure, as shown in Fig. 19, with a low-current electron beam in a CRT. Our calculations for such a cavity indicate that a pair of deflection cavities like those in Fig. 19 could result in double the power gain of the prototype gyrocon. The gain is only doubled because the TE cavity has very low loss, but very high beam loading, whereas the TM cavity has approximately equal amounts of power in the rf losses and in beam loading. Higher gain gyrocons with TE cavities may well be possible, but we have not found them with our codes. If one had a low-current, low-perveance gyrocon the TE deflection cavity would give high gain, but then the output losses would be very large and the overall efficiency would not be high. Wessel-Berg[15] claims that high-gain, high-efficiency gyrocons

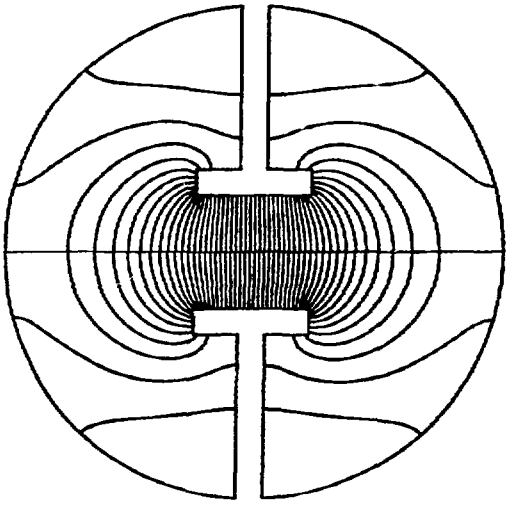

Fig. 19. A TE deflection cavity studied with the code SUPERFISH. Major diameter = 30 cm, resonant frequency = 440 MHz.

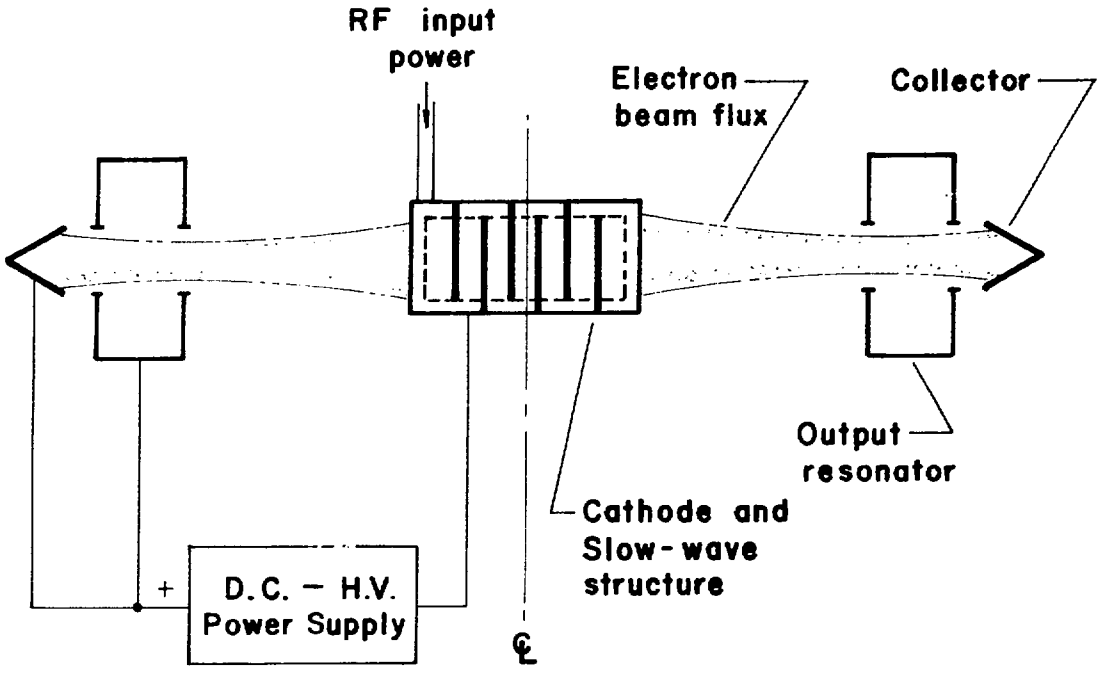

Fig. 20. The planar gyrocon.

can be made with TE deflection cavities, and this approach should be examined more carefully in the future.

The best performance for the gyrocon family in the 2- to 4-GHz frequency range may be possible only by eliminating the deflection system as well as the bender solenoid. Figure 20 shows schematically one embodiment of this idea that we call the planar gyrocon. The cathode now must have a rotating emissive area; thus no deflection cavities are required. The plate supply pulls the electron to the output cavity, where the energy extraction takes place. The difficult part of this arrangement is the electron gun. One possible solution to this problem is the inverted Amplitron gun,[16] which utilizes a slow-wave structure made of secondary emitting materials as the cathode. Another possible solution to the planar gun problem is to use a multipactor electron gun,[17] which in the multipactor region moves in a slow-wave or waveguide structure. Still another possibility is to use a thermionic cathode as part of a waveguide. A traveling wave in the input waveguide could control the electron flow to the output waveguide in much the

same manner as the control grid in a triode. Lebacqz,[18] the originator of this last method, calls this dual-waveguide version of the planar gyrocon a trirotron. At this time the authors will not speculate on which embodiment of the planar gyrocon will prove optimum, but they feel that at least one of these will be practical as a high-efficiency amplifier in the 2- to 4-GHz range. At these high frequencies, it would probably be best to build the planar gyrocon in the inverted configuration, with the cathode surrounding the output cavity.

VII. SUMMARY AND CONCLUSIONS

A type of deflection-modulated microwave amplifier has been analyzed in this paper. This device has a long history, but only recently has it been demonstrated successfully as a highly efficient rf power amplifier. A large-signal, three-dimensional analysis that includes first-order space-charge and relativistic effects is presented. The results indicate that electronic efficiencies of over 90%, and overall efficiencies approaching 90%, should be achievable at frequencies below 3.0 GHz. The rf gain and conversion efficiency increase as the beam power is increased, making the device well suited for high-power applications. The bandwidth of the gyrocon is very narrow because the Q of the input resonator is about 20 000. The bandwidth of the output cavity is also fairly narrow, but this cavity has a loaded Q of ~ 1000. The effects of a mismatch or of frequency deviations from resonance in the output cavity may be analyzed with resonant-ring theory.[19] The output power and high-frequency limitations of the gyrocon arise from the finite size of the beam and the ohmic losses in the output resonator. The authors estimate that the device can be competitive with klystrons and crossed-field devices, up to frequencies of 3 GHz. The low-frequency limit to the gyrocon must be rather close to the 181-MHz, 5-MW cw Soviet machine, which is 4.25 m tall and weighs over 5 000 kg. The rf gain of the gyrocon is between 10 and 25 dB for the examples calculated here, but the authors expect that the supplementary deflection cavities of Fig. 15 should add another 10 to 20 dB.

The present analysis indicates that the gyrocon amplifier should be considered for multimegawatt, narrow-band microwave systems that operate below approximately 3 GHz. In such applications, the excellent dc-to-rf conversion efficiency and the large power available per device should overcome its narrow

bandwidth and rather modest gain limitations. If its planar variant can be produced, the gyrocon could be made in a much simpler manner and then it would become a lightweight device that could be useful for high-power airborne or space applications of microwaves.

APPENDIX A

SPACE-CHARGE CALCULATION

A detailed calculation of space-charge effects in the gyrocon would involve following the three-dimensional motion of a considerable portion (many disks) of the charge in the beam, and the use of a Green function for the fields based on the overall geometry. Alternatively, some sort of mesh system can be set up and Poisson's equation solved at each step. However, this still involves a three-dimensional analysis. Thus, to facilitate the space-charge simulation, the free-space Green function is used. Furthermore, the beam space-charge fields are derived from a rod approximation of the beam, which in turn is constructed from the motions and locations of the components of a single layer of the beam. The problem is thus simplified considerably.

The model is essentially nonrelativistic in that the electric field produced by each rod is calculated from Coulomb's law,

$$\vec{E}_{rod} = \frac{\lambda_{rod}}{2\pi\epsilon_o} \frac{\vec{r}}{r^2} , \tag{A-1}$$

the standard electrostatic expression[20] for a line charge of density λ_{rod}. The magnetic field is calculated as

$$\vec{B}_{rod} = \vec{v}_{rod} \times \vec{E}_{rod}/c^2 , \tag{A-2}$$

a result that is valid even at relativistic velocities provided $\vec{E}_{rod}$ is relativistically correct.[21]

The most unusual feature of the rod model of the beam is that the rods constructed as an approximation to the beam will in general not lie along the beam velocity. Rather, they must be constructed to lie along the tangent to the helix that the beam appears to form at any given time. This allows a

simulation of the three-dimensional beam by use of a two-dimensional, approximate model that changes its spatial orientation as necessary, as the beam electrons move.

A. Construction and Use of Rods in the Model

Because the computer code follows a single layer of electrons by numerical integration as they pass through the system, it is necessary to construct the rod model from the information in the motion of this single layer. For simplicity we consider only the motion after the layer has been deflected from its original axial motion. The axial motion case can then be recovered as a limiting case of this more involved motion by setting $\omega = 0$.

At any given point in the numerical integration of the motion, the computer code has available all of the current positions and velocities of the subdivisions of the layer being followed. The position of one of these sections, at the immediately preceding integration step (time Δt earlier), is also available. The section whose preceding position is stored is called the reference particle, and its selection can be (and is) varied among all the sections of the layer, over a cycle of integration steps.

The space-charge routine assumes that at the current point in time, there exists a second layer of charge emitted at a time Δt earlier, which has duplicated the motion of the layer being followed except for a time lag of Δt, and most importantly, an angular offset equal to $\omega\Delta t$ is caused by its later passage through the deflection cavity. Thus, the reference particle in the second layer is assumed to lie currently at the previous, main-layer, reference-particle location, offset by angle $\omega\Delta t$.

The tangent to the physical helix that the beam appears to form is now considered to lie along the vector joining the two reference particles. To illustrate this, the current position of the reference particle at point P, its earlier position at point P', and the derived, second, reference particle at point P'' are all shown in Fig. A-1 in exaggerated scale.

Also shown are the distances ℓ' and ℓ that would lie between reference particles in the deflected and undeflected beams, respectively. The values are related by

$$\ell' = \ell/\cos\theta \quad , \tag{A-3}$$

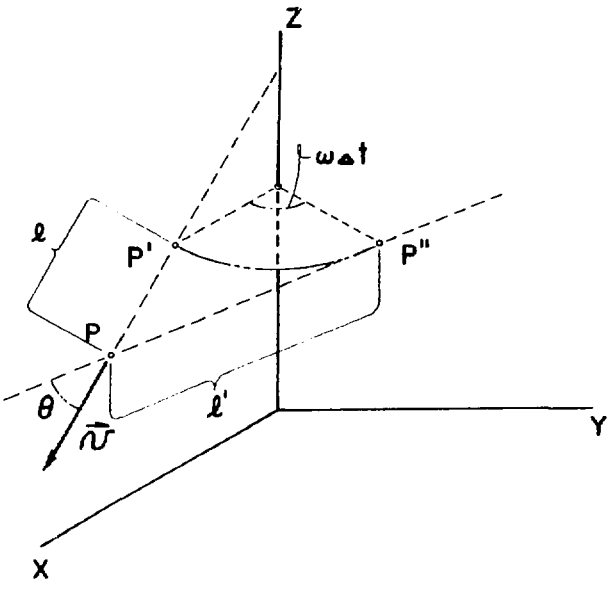

Fig. A-1. Construction of the helix tangent to the reference particle.

and because the charge in the beam is stretched over the distance ℓ', the effective charge density of any rod is reduced by the factor cos θ from what it would be in the undeflected beam.

The rods are now constructed through each current particle position in the main layer with directions parallel to the constructed tangent. This is done by constructing a plane perpendicular to the tangent and through the current reference particle. All the other particles are then projected normally onto this plane. Thus, the situation for the particle, and two other particles, might appear as shown in Fig. A-2.

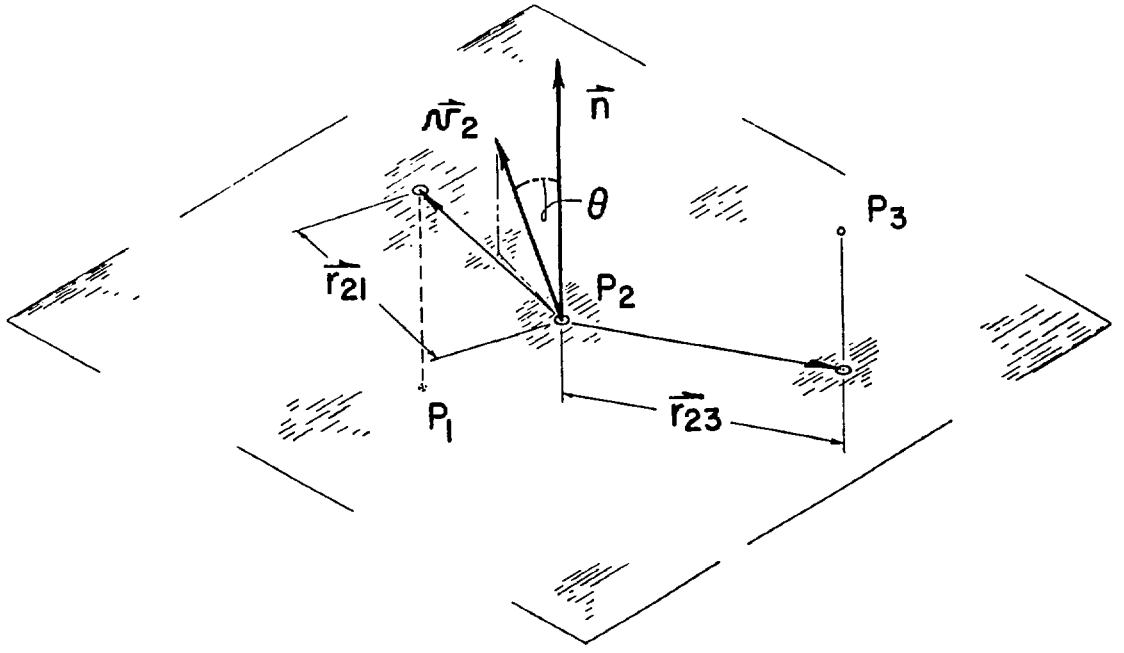

Fig. A-2. Projection of the particle positions.

The space-charge electric field at particle 3 that is due to particle 2 is now computed by Coulomb's law to be

$$\vec{E}_{SC_{32}} = \frac{\lambda_2 \cos \vec{\theta}\, \vec{r}_{23}}{2\pi\varepsilon_o r_{23}^2} \quad , \tag{A-4}$$

where λ_n is the linear charge density associated with particle n according to

$$\lambda_n = \frac{I_n}{v_{o_n}} \frac{\bar{v}_o}{\bar{v}} \quad . \tag{A-5}$$

Here the quantities

I_n = initial current in beam section n,

v_{o_n} = initial value of speed for section n at injection,

$\bar{v}_o$ = average injection speed of all sections, and

$\bar{v}$ = current average speed of all sections.

The factor $\bar{v}_o/\bar{v}$ is a correction to all the charge density to the increase as the electrons slow down and pile up. The full space-charge field at particle i is

$$\vec{E}_{SC_i} = \sum_{j \neq i} \vec{E}_{SC_{ij}} \quad . \tag{A-6}$$

This vector is applied at the actual position of the particle. Likewise $\vec{B}_{sc_i}$ is constructed from

$$\vec{B}_{SC_i} = \sum_{j \neq i} \vec{B}_{SC_{ij}} \quad , \tag{A-7}$$

where

$$\vec{B}_{SC_{ij}} = \vec{v}_j \times \vec{E}_{SC_{ij}}/c^2 \quad . \tag{A-8}$$

Note that although the factor cos θ in Eq. (A-4) tends to reduce space-charge effects, the projecting onto the plane tends to cancel this effect by moving the rods closer to each other. Also, the direction of E_{sc} is always normal to the constructed tangent, rather than to the direction of particle velocity.

B. Projection Formulas

Given the cylindrical coordinates of the reference particle (1) as (r_1,ϕ_1,z_1), the previous position Δt earlier as (r_1', ϕ_1', z_1'), and a second particle (2) currently at (r_2, ϕ_2, z_2), the projected location of the particle (2) is given by

$$r_3 = \left[(r_2 - \tau s)^2 + \sigma^2 s^2\right] , \tag{A-9a}$$

$$z_3 = z_2 - \gamma s \quad , \tag{A-9b}$$

$$\phi_3 = \phi_2 \arctan \frac{\tau s}{r_2 - \tau s} \quad , \tag{A-9c}$$

where

$$s = \frac{r_2(\alpha^2 + \beta^2)^{1/2} \cos (\phi_0 - \phi_2) - \alpha r_1 + \gamma(z_2 - z_1)}{\gamma^2 + (\alpha^2 + \beta^2)^{1/2}\left[\alpha \cos (\phi_0 - \phi_1) + \beta \sin (\phi_0 - \phi_1)\right]} \quad , \tag{A-10a}$$

$$= \alpha \cos (\phi_1 - \phi_2) - \beta \sin (\phi_1 - \phi_2) \quad , \tag{A-10b}$$

$$\sigma = \alpha \cos (\phi_1 - \phi_2) + \beta \cos (\phi_1 - \phi_2) \quad , \tag{A-10c}$$

$$\phi_0 = \phi_1 + \arctan (\beta/\alpha) \quad , \tag{A-10d}$$

$$\alpha = r_1 - r_1' \cos (\phi_1 - \phi_1' - \omega\Delta t) \quad , \tag{A-10e}$$

$$\beta = r_1' \sin (\phi_1 - \phi_1' - \omega\Delta t) \quad , \tag{A-10f}$$

and

$$\gamma = z_1 - z_1' \quad . \tag{A-10g}$$

The arctangents must be chosen in the correct quadrants for the numerator of the argument to be the sine of the result, and the denominator to be the cosine. Also, when working in cylindrical coordinates care must be exercised in transplanting calculated fields from projected positions to actual ones (components will change). Finally, rather than use the actual particle velocity v_j of the jth particle in Eq. (A-8), the velocity vector is rigidly rotated to the projected position through any separating angle. This is equivalent to preserving the numerical values of the velocity components of the particle from its original, nonprojected position. This assumes that the rod at the projection plane would actually have a velocity rotated slightly from that of the nonprojected particle.

C. Relativistic Corrections

Though not present in the results reported here, corrections do occur in Eq. (A-4) for highly relativistic beams. In such cases, if one ignores acceleration fields then Eq. (A-4) can be written

$$\vec{E}_{SC_{32}} = \frac{\lambda_2 \cos \theta}{2\pi\epsilon_0 \sqrt{\xi_2}} \quad \frac{\vec{r}_{23} - \beta_2^2 \vec{C}_{23}}{\eta_2 \, r_{23}^2} \quad , \tag{A-11a}$$

$$\xi_2 = 1 - \beta_2^2 + \frac{(\vec{v}_2 \cdot \hat{n})^2}{c^2} \quad , \tag{A-11b}$$

$$\eta_2 = \xi_2 + \frac{(\vec{v}_2 \cdot \vec{r}_{23})^2}{c^2 \, r_{23}^2} \quad , \tag{A-11c}$$

$$\beta_2 = \frac{v_2}{c} \quad , \tag{A-11d}$$

$$\hat{n} = \text{unit tangent vector to helix} \quad , \tag{A-11e}$$

$$\vec{C}_{23} = \frac{\vec{v}_2 (\vec{v}_2 \cdot \vec{r}_{23}) \, (\vec{v}_2 \cdot \hat{n})^2}{v_2^4} + \left[\vec{r}_{23} \, \alpha_2 + \frac{\vec{n} (\vec{v}_2 \cdot \vec{r}_{23}) \, (\vec{v} \cdot \hat{n})}{v_2^2} \right] \alpha_2 \quad , \tag{A-11f}$$

and

$$\alpha_2 = 1 - \frac{(\vec{v}_2 \cdot \hat{n})^2}{v_2^2} \quad . \tag{A-11g}$$

These equations are derived by considering the electric field seen at an observation point (3) at a normal distance $\vec{r}_{23}$ from a rod of charge in the laboratory frame. The rod lies along vector $\hat{n}$, has a charge density $\lambda_2 \cos\theta$, and a velocity $\vec{v}_2$ (assumed constant), all in the laboratory frame. The derivation involves Lorentz transforming to the rest frame of the rod, calculating the electric field at point (3) in that frame, using Coulomb's law, and then performing the reverse Lorentz transformation to the laboratory frame on the electric field.

Some preliminary tests of these equations in a separate, modified gyrocon code, using the LASL prototype gyrocon parameters, seem to indicate that these changes cause only a few-tenths per-cent shift in overall efficiency. This might be expected because the LASL prototype has an electron beam whose velocity is only about half the speed of light.

Also, direct calculation of just the space-charge fields with a simulated beam seems to indicate that space-charge fields tend to increase, on the average, over nonrelativistic values for highly relativistic beams. The effect is most marked in directions normal to the beam velocity, but even the leading and trailing helix edges experience a net increase in space-charge fields.

APPENDIX B

PREPARATION OF INPUT DATA FOR GYROCON COMPUTER CODES

GYRO1 and GYROS are programs for analyzing the electron dynamics in all the regions of the rectangular and spherical gyrocon. Space charge is included, and one may use the code to analyze drift spaces, deflection cavity, bender region, output interaction region, and collector drift space. The data files must be set up as follows.

File Input

Card 1.	Format	6E6,3I2
1-6	FMHZ	The frequency in MHz. If zero, the run stops.

7-12	VA	The anode voltage of the gyrocon, V.
13-18	Iø	The beam current, A.
19-24	RMAX	The radial extent of the problem, m.
25-30	ZMAX	The z boundary of the problem, m.
31-36	BøA	The ratio of initial beam radius to drift tunnel radius, set to 0.7 if left blank.
37-38	M	The input beam parameter. M=00 is for an ideal, laminar beam-generated GYRO1. M=01 causes GYRO1 to read TAPE20 for the output of a SLAC electron gun run that is used for the input beam.
39-40	M1	The region parameter. Starting at the input beam, the calculation ends at • the end of the first drift space if M1=01, • the end of the deflection cavity if M1=02, • the end of the bender space if M1=03, or • the end of the output cavity if M1=04 or M1=05. M1=05 is a special value that causes TAPE3 to be read for the output cavity card (or cards) rather than file INPUT. This useful feature is explained more fully under Output-Cavity Cards.
For GYROS only:		
41-42	M0	The order of frequency multiplication in the output cavity, 00 or blanks defaults to 01.
Card 2.	Format	1012
1-2	ISC	The space-charge parameter. ISC=00 ignores all space charge. ISC=01 calculates electric fields only. ISC=02 calculates electric and magnetic fields. ISC=03 includes higher order relativistic effects in the electric and magnetic fields.

3-4	IPR	The number of time steps per print-out on TAPE12, the major output file.
5-6	IJPR	Not used.
7-8	ITY	Switch for teletype plot - a picture appears if ITY>00. Also, if ITY=02 extra plots are included on the film file (see cavity plot cards).
9-12	IPLT	The number of time steps per plot interval-- remember we only plot 1000 points.
13-14	ITEST	A test switch to generate diagnostic prints. ITEST=00 and 01 gives minimum print-out on TAPE12. ITEST=02 gives the E fields and B fields at each print step. ITEST=03 prints output gap fields at each print step.
15-16	IMLT	A multiplier that is applied to the values of IPR and IPLT after they are read. This value is reset to 01 if it is less than 01 or is blank.
17-18	IGR	A switch to turn all film-file plotting off. 00 or blanks leave it on, whereas any other value turns it off. Note that this switch may be reset from output cavity cards (see them).
19-20	ISPR	A switch to mimic superconducting cavities (divides resistivity by 10^6) if not 00 or blanks.
21-22	IRECT	A switch for rectangular coordinates IRECT > 0 forces rectangular coordinate force equations.

Card 3.	Format	7E6
1-6	R_ϕ	The initial beam radius, m.
7-12	ANG	The convergence of the ideal beam, deg.
13-18	DSZ	The distance step used in the calculation, m.
19-24	Z1	The axial location of the start of the deflection cavity, m.

25-30	Z2	The end of the deflection cavity, m.
31-36	Z_{ϕ}	A number to be subtracted from the z coordinate of the SLAC electron gun program in meters.
37-42	K	The cathode flux parameter for the ideal beam case.

Card 4.	Format	6I2
1-2	NR	The number of rings the beam is divided into.
3-4	NT	The number of beamlets each ring is divided into. Note NRxNT < 50.
5-6	NC	The number of current loops (coils) in the problem. NC < 50.
7-8	NRM	The number of rows in the radial magnetic mesh. NRM < 50.
9-10	NZM	The number of columns in the axial magnetic mesh. NZM < 100.

For GYROS only:

11-12	ICSP	A flag indicating, if blanks, 00 or 02, that the last two coils specified on coil cards are in a special format using spherical coordinates and relative to the output-cavity beam-slot position. This is only valid when M1 > 2. Also there must be at least two coils present or no coils at all.

If NC > 0, NC coil cards are read as follows:

Coil Cards	Format	3E6
1-6	ENI	The number of ampere turns in the coil.
7-12	RC	The coil radius, m. A zero here terminates this set of input data. (Next card is card 1.)
13-18	ZC	The axial location of the coil, m.

The last two coils are always used as the output-cavity focus coils if any special focus-coil operations are performed (such as special plots when ITY = 2).

For GYROS only:

If M1 > 2 and ICSP = 0 or 2, then the last two coils are entered in a special format.

1-6	ENI	Same as above.
7-12	RC	On the next to last card, the radial distance of both focus coils from the origin of spherical coordinates if ICSP = 00. (See ZCEN below.) Or if ICSP = 02, the radial distance of both focus coils inside the output-cavity inner wall (R1). On the last card this field can have any non-zero value and is otherwise ignored.
13-18	ZC	On the next to last card, the linear separation of the two coils. This field is ignored on the last card.

The above special format for the last two coils is then translated by the program into a true cylindrical coordinate RC and ZC for each coil based on the calculated output-cavity beam-slot location. The coils straddle the slot center angle (which may differ from the cavity center angle). ICSP = 01 causes the coils to be handled in straight cylindrical coordinates.

If M1 > 1 the next card is the Deflection Cavity Card. Format 3E6

1-6	ED	The deflection field, MV/m.
7-12	DTD	The rf time step, deg.
13-18	TOD	The phase angle of the rf field, deg.

If M1 > 2 the next card is the Bender/Output Card. Format 3E6, 3I2, 2E6

1-6	Z3	The z-plane that is the end of the problem region, m.
7-12	R1	The inner radius of the output waveguide, m.
13-18	R2	The outer radius of the output waveguide, m.
19-20	NOR	The number of entries in the radial function tables for the output fields. NOR < 50.
21-22	ISCO	The ISC parameter for the output calculation.

For GYRO1 only:

23-24	NLG	The number of wavelengths in the output guide. Default is one.

For GYROS only:

23-24	NOTH	The number of entries in the angular (theta angle) function tables for the output fields. NOTH < 50.
25-30	ZCEN	The z-coordinate in cylindrical coordinates of the origin of the spherical coordinates used for the output cavity and possibly the focus coils (see ICSP). The spherical theta angle is measured from the positive z-axis.
31-36	CENA	The theta angle of the output-cavity physical center, deg.

If M1 = 4 the next card is read from file INPUT (this data file). If M1 = 5 the next card is read from file TAPE 3. The card is the Output Gap Card. Format 2E6, I2, E6

1-6	EOO	The radial electric field at the inner surface of the output guide, MV/m.
7-12	THOD	The phase angle of the output field, deg.
13-14	IGRA	A plot control switch. A -1 here resets IGR (see card 2) to off, a + 1 resets it to on, and any other value (including blanks) leaves it unchanged.

For GYROS only:

15-20	BST	Controls a static magnetic field in the theta direction in the output cavity. This value is the fraction of the peak theta rf magnetic field that will be used as the value of a static, theta, magnetic field. Blanks or zero mean no static field.

If M1 = 5 and for any reason film plotting is set off as the program finishes the output loop (or earlier if a plot overflow occurs), the program will read an extra card on TAPE3 for final plot control.

Plot Control Card. Format I2

1-2	IGRB	Any non-zero value turns on plotting. (See Additional Notes.)

If ITY = 02 (see card 2) and either M1 > 3, or M1 < 3 together with IGR on (or IGRA or IGRB), then two more cards are read (at the back of file INPUT). They are:

Plot Specification Cards. Format 4E6, I2

1st Card:

1-6	RP1	The cylindrical r-coordinate of the outside of the top of the bender.
7-12	RP2	The cylindrical r-coordinate of the outside of the bottom of the bender.
13-18	RP3	If IPF = 00, the cylindrical (GYRO1) or spherical (GYROS) radius of the inner lip of the inside output-cavity slot. If IPF ≠ 00, the distance of the inner lip inside the inner cavity wall (R1).
19-24	RP4	If IPF = 00, the cylindrical (GYRO1) or spherical (GYROS) radius of the outer lip of the outside output-cavity slot. If IPF ≠ 00, the distance of the outer lip outside the outer-cavity wall (R2).

25-26	IPF	A flag to designate whether RP3 and RP4 are measured from the cavity walls (IPF = 00, recommended) or from the same origin as R1 and R2 (IPF = 00 or blank).

In GYROS for M1 < 3, the spherical coordinate system origin ZCEN will default to zero, and RP3 and RP4 (or R1 and R2) are measured from such.

2nd Card:

1-6	ZP1	z-coordinate of the top of the bender.
7-12	ZP2	z-coordinate of the bottom of the bender.
13-18	ZP3	The linear distance inward from a focus coil center to the output-cavity slot lip that supports it. This distance is measured along the line between focus coils and obviously requires their presence. If no actual focusing is desired, their ENI values (see coil cards) should be set to values much less than 1, for example, 0.0001, etc.

These plot specification cards allow an outline of the output cavity and bender cone to be traced on the second film plot. In GYROS, inner- and outer-cavity slots are assumed to be the same linear size, and the focus coils are assumed inside the cavity's inner wall.

Additional Notes

The use of M1 = 05 allows semiconversational output-cavity specification. Under NOS the user may enter (assuming binary deck BGS)

```
/BGS, DATA, TAPE20, INPUT
```

where DATA is an input file with M1 = 5 and no output gap cards (but including plot specification cards, if any). The program will run up to the output gap and then issue (at the terminal)

?

at which point the user types the output gap card at the terminal. If film plotting is off, a second

?

is issued after the cavity is integrated to allow plotting to be turned on. Following this another

?

is issued to run another output gap section of the code with the same injection into the gap but different gap parameters.

The above cycle continues until an EOO of 0 is encountered, at which point the program terminates.

Note: GYROS terminates after one film plotting without allowing further loops. The above multiple runs of an output gap are only allowed as long as film plotting is kept off.

For M1 < 5, either program will attempt to read a second complete set of input data for a second entire run. However, a frequency (FMHz) of zero will stop the run.

Figure B-1 shows a data form the authors use to set up data sets for GYRO1 and GYROS.

GYRO1 AND GYROS INPUT FILES

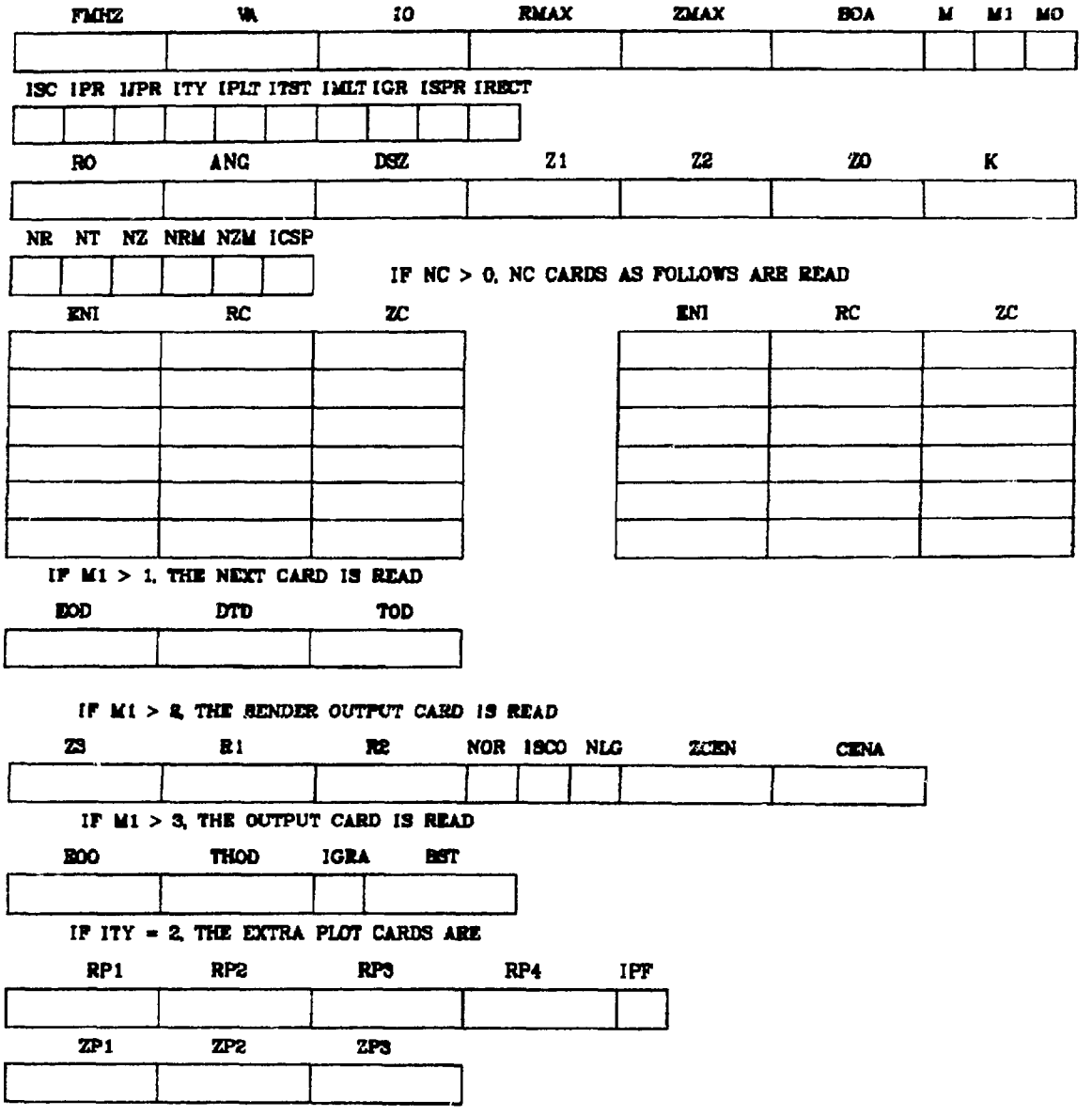

Fig. B-1. Data form used to set up input files for GYRO1 and GYROS.

REFERENCES

1. P. J. Tallerico, "The Gyrocon, A Deflection-Modulated, High-Power Microwave Amplifier," Los Alamos Scientific Laboratory report LA-6907, October 1977.

2. P. J. Tallerico, "A Class of Deflection Modulated, High-Power Microwave Amplifiers," 1977 International Electron Device Meeting Technical Digest, pp. 242-245, Washington, D.C., December 1977.

3. G. I. Budker, M. M. Karliner, I. G. Makarov, S. N. Morozov, O. A. Nezhevenko, G. N. Ostrieko and I. A. Shekhtman, "The Gyrocon, A Highly Efficient Converter of Energy from Powerful Relativistic Beams for Microwave Supplies in Charged-Particle Accelerators," Atomic Energy, Vol. 44, No. 5, pp. 459-466, May 1978.

4. G. I. Budker, M. M. Karliner, I. G. Makarov, S. N. Morosov, O. A. Nezhevenko, G. N. Ostreiko and I. A. Shekhtman, "The Gyrocon--An Efficient Relativistic High Power VHF Generator," Particle Accelerators, Vol. 10, pp. 41-59, 1979.

5. G. I. Budker et al., "The rf System of the VEPP-4 Electron-Position Storage Ring Based on the Gyrocon--A High-Power UHF Generator with an Unbunched Relativistic Beam," Dubna Accelerator Conf. Proc., Dubna U.S.S.R., October 1976. (Available in English as SLAC Trans-177, SLAC, August 1977.)

6. P. J. Tallerico and J. E. Rankin, "Computer Modeling of the Gyrocon," IEEE Trans. on Nuclear Science, Vol. NS-26, No. 3, pp. 4015-4017, June 1979.

7. P. J. Tallerico and J. E. Rankin, "The Gyrocon; A High Efficiency, High-Power Microwave Amplifier," IEEE Trans. on Electron Devices, Vol. Ed-26, No. 10, pp. 1559-1566, October 1979.

8. J. E. Rankin and P. J. Tallerico, "S- Band Microwave Power Generation with Spherical Gyrocons," submitted to the Space Solar Power Review, February 1980.

9. R. F. Harrington, Introduction to Electromagnetic Engineering, McGraw-Hill, New York, 1958, pp. 130-133.

10. J. R. M. Vaughan, "Representation of Axisymmetric Magnetic Fields in Computer Programs," IEEE Trans. on Electron Devices, ED-19, pp. 144-151, February 1972.

11. A. N. Winslow, "Numerical Solution of the Quasilinear Poisson Equation in a Nonuniform Triangle Mesh," Journal of Computational Physics, Vol. 2, pp. 149-172, 1967.

12. W. B. Herrmannsfeldt, "Electron Trajectory Program," Stanford Linear Accelerator Center publication SLAC-166 (1973).

13. S. A. Schelkunoff, Electromagnetic Waves (D. Van Nostrand Co., Princeton, 1943), pp. 399-450.

14. T. Kageyama, Y. Morizumi, and E. Watanabe, "A Large-Signal Analysis of Broad-Band Klystrons with Design Applications," IEEE Trans. in Electron Devices, Vol. Ed-24, pp. 3-12, Jan. 1976.

15. T. Wessel-Berg, "A New Concept for Generation of Multi-Megawatt Power Approaching Hundred Percent Conversion Efficiency," Technical Digest, IEEE 1977 International Electron Devices Meeting, Washington, DC, pp. 238-241, Dec. 1977.

16. G. MacMaster and L. Nichols, "High Gain Crossed Field Amplifier Tube," Paper 12.4, Technical Digest, 1977 International Electron Devices Meeting, pp. 245B, Dec. 1977, Washington, D. C.

17. D. J. Liska, "Multipactoring Electron Gun for High Duty Linacs," Proc. IEEE, Vol. 59, pp. 1253-1254, August 1971.

18. J. V. Lebacqz, A. J. Dudas, and W. R. Fowkes, "The Trirotron," IEEE Trans. Nucl. Sci., Vol. NS-26, pp. 3891-3893, June 1979.

19. W. R. Fowkes and P. B. Wilson, "Application of Traveling Wave Resonators to Superconducting Linear Accelerators," IEEE Trans. of Nucl. Sci., NS-18, pp. 173-175, June 1971.

20. W. K. H. Panofsky and M. Phillips, Classical Electricity and Magnetism, Addison-Wesley Publishing Co., Inc. Reading, Mass., pp. 64-65.

21. L. D. Landau and E. M. Lifshitz, The Classical Theory of Field, Pergamon Press, Addison-Wesley Publishing Company, Inc., Reading, Mass., pp. 68-70, 1962.

☆ U.S. GOVERNMENT PRINTING OFFICE: 1980—677-115/183